ARTICLE
DOI: 10.1590/2317-4889202020180128

BJGEO Brazilian Journal of Geology

Genesis of the "soft" iron ore at S11D Deposit, in Carajás, Amazon Region, Brazil

Aline Cristina Sousa da Silva[1]*, Marcondes Lima da Costa[1]

Abstract
The origin of the soft ore at the S11D iron mine in Carajás was investigated using 20 samples from a diamond drill hole. The methods of analyses were X-ray diffraction (XRD), optical microscopy, whole-rock chemistry, and scanning electron microscope coupled with energy-dispersive X-ray spectroscopy (SEM/EDS). The drill hole presents a profile through the substratum (protore, a banded iron formation — BIF) and three weathering horizons, defined from the base to the top, saprolite (coarse and fine), and crust. The soft iron ore occurs distributed along the saprolite horizon, and it is composed mainly of hematite and subordinate magnetite. The amount of quartz decreases upwards, whereas the amount of Fe-Al-(Ti-P)-minerals increases towards the top. The total iron is enriched in the fine saprolite when compared to the protore (42.55 to 97.62 wt.% Fe_2O_3, respectively). Trace elements such as Zr, Cr, Y, and rare earth elements (REE) show relative enrichment upward because they are generally located in residual minerals (as zircon and anatase). The REEs in iron ore samples exhibit enrichment of light rare earth elements (LREE) and depletion of heavy rare earth elements (HREE), with pronounced positive Eu anomaly, which reaffirms the connection between iron ore and BIF. Based on the mineralogy, chemistry, textures, and structures, a genetic laterite-supergene model is proposed for the origin of soft ore at the S11D deposit.

KEYWORDS: Banded iron formation-protore; lateritic profile; hematite; magnetite; geochemistry.

INTRODUCTION

The present work has investigated the S11D iron ore deposit located at the Carajás Mineral Province (CMP) (Grainger *et al.* 2008), Serra Sul, southeast of Pará state, Brazil (Fig. 1). The CMP hosts many iron ore deposits, estimated to contain 17 billion tons of iron (Vale 2017). Only the iron ore deposits at Serra Sul are estimated to contain 4.3 billion tons, with more than 66.7 wt.% Fe content (Vale 2017). The production of iron ore from the N5 (N5E and N5W), N4 (N4E, N4W, N4C) and S11D deposits was 169.2 million tons in the second part of 2018 (Vale 2018).

Although this region has high investments in mineral exploration, mainly by Vale S.A., the geological knowledge is still limited. Considering the lack of information about the origin of the soft iron ore derived from the banded iron formations (BIFs) of the Carajás Formation, the aim of this paper was to provide geologic, mineralogic and chemistry data of soft ore, focusing on its relationship to a laterite-supergene profile, which is exemplified in the S11D deposit.

This paper consists of a petrological and geochemical study, using mineralogy, whole-rock chemical composition, and mineral chemistry. It intends to:

- characterize the mineralogy in each horizon;
- define the relationship between ores and protore;
- define affinity between the newly formed and inherited minerals;
- propose a genetic chronology of events considering textures, structures, mineralogy and chemical composition of each horizon in the profile;
- discuss the processes and evolution that lead led to the formation of each horizon;
- propose a model for the laterite-supergene iron ore profile.

The contribution of laterite weathering has been demonstrated by Costa (1991), Costa *et al.* (2005a), Horbe and Costa (2005), Costa *et al.* (2009), Costa *et al.* (2011), Costa *et al.* (2014), Santos *et al.* (2016), Costa *et al.* (2016), and Oliveira *et al.* (2016). Also, these authors described the intense weathering due to the lateritization process and intense erosional activity in the ore deposits located in the Carajás and Amazon region. Vasconcelos *et al.* (1994) showed that lateritic weathering had affected the region for the last 70 Ma with some hiatus.

GEOLOGICAL SETTINGS

The iron ore deposits show strong relationship to the special distribution of the BIF of the Carajás Formation (2.7 Ga), an intermediate unit of the Grão Pará Group (GPG) (Fig. 1). The contacts between the wall-rocks and BIF are concordant and tectonic (Silva 2014) (Fig. 2). The BIF is positioned above the Parauapebas Formation (basalts and rhyolites),

[1]Universidade Federal do Pará – Belém (PA), Brazil.
E-mails: alinecs.silva@hotmail.com, mlc@ufpa.br
*Corresponding author.

and below the mafic and sedimentary rocks of the Igarapé Cigarra Formation (Grainger *et al.* 2008, Vasquez *et al.* 2008a, Dall'Agnol *et al.* 2013, and Silva 2014).

The BIF is characterized by irregular and discontinuous intercalations of quartz/chert microbands and iron oxides, showing primary and depositional structures (Lindenmayer *et al.* 2001, Macambira & Schrank 2002). The content of iron in BIF ranges from 17.11 to 43.40 wt.% Fe_2O_3 and 35.10 to 60.84 wt.% SiO_2 (Meirelles 1986). A volcanogenic origin for these BIF is indicated by Meirelles (1986), Dardenne and Schobbenhaus (2001), and Klein and Ladeira (2002) based on the GPG environment and the geochemical characteristics of the BIF (Figueiredo e Silva *et al.* 2011).

There are two types of hematite ores hosted in the Carajás Formation, the soft (*i.e.*, high porosity) and the hard (*i.e.*, low porosity). The soft hematite ore represents the main orebody of iron ore in Carajás (Fig. 2), with 64 to 67 wt.% Fe_2O_3 (Rosière & Chemale Jr. 2000). At the N4E mine, for example, the high-grade ore body is 100 to 400 m thick, crosscut by dikes and sills of mafic rocks (Klein & Ladeira 2002). The soft ore was considered by Tolbert *et al.* (1971) as a product of supergene enrichment after the dissolution of silica.

The hard iron ore has tabular or lenticular shape, discordant with the soft ore, concentrated near the contact with the lower metabasic rocks, and represents less than 10% of the resources (Dalstra & Guedes 2004). The hydrothermal contribution to the formation of the hard ore is characterized by quartz recrystallization, removal of Fe and the formation of magnetite associated with microcrystalline hematite, associated with quartz and carbonate veins (Figueiredo e Silva *et al.* 2008, Figueiredo e Silva *et al.* 2013). The hard ore will not be discussed in this paper.

MATERIALS AND METHODS

The drill hole (SSDFD663) studied comprises 524.5 m (-84.84º/165.38º direction) and has been located at the S11D

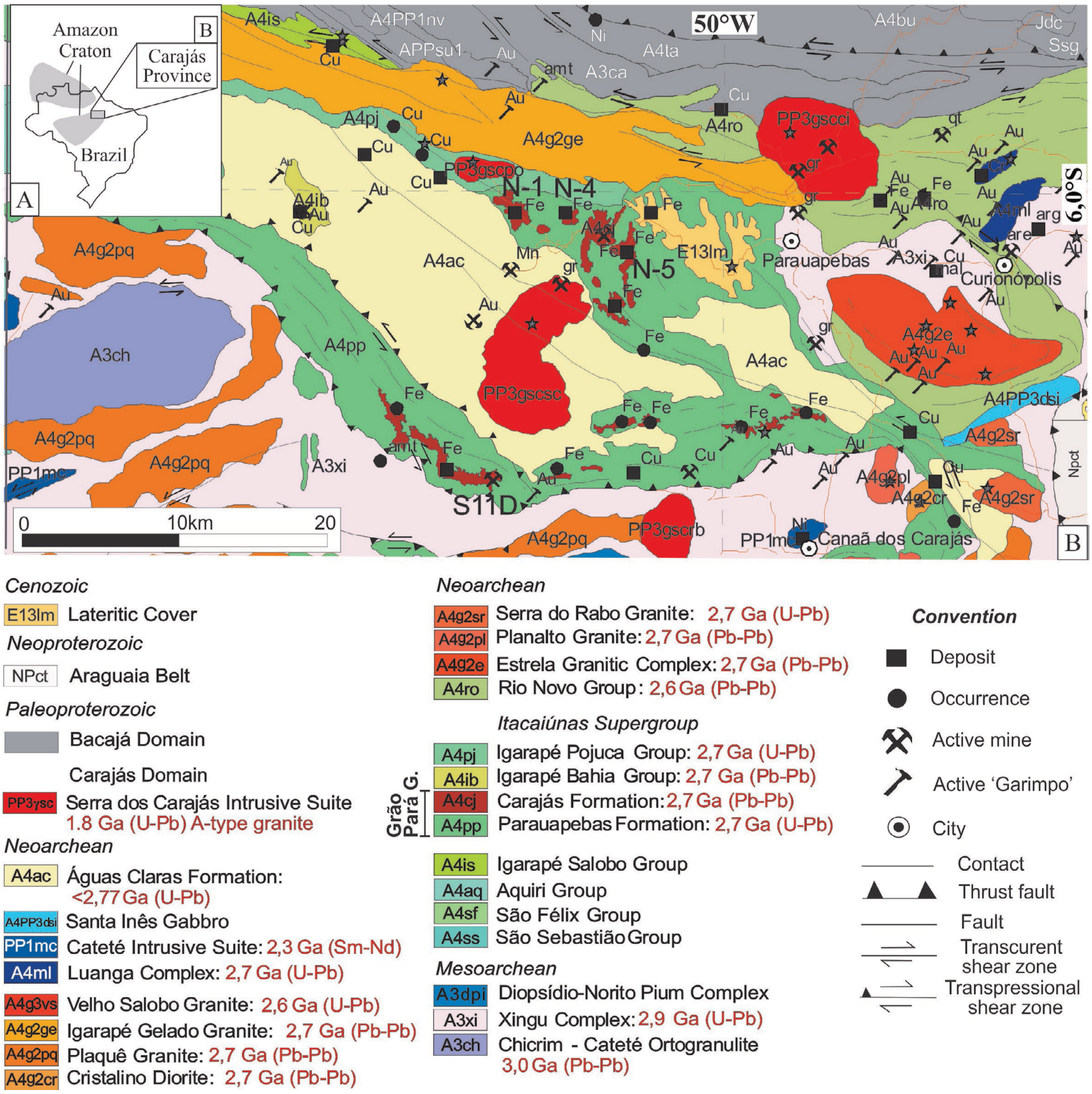

Source: modified after Vasquez *et al.* (2008b).

Figure 1. Geological map of Carajás. (A) Brazil and the Amazon Craton. (B) The Carajás Province.

iron mine (UTM 576.320.847/9292204.02). It was chosen because of its complete weathering sequence, within defined horizons. Fifty-five samples were collected for mesoscopic study at different depths, numerated from the top to the bottom. Due to its similarities, only 20 samples representative of the minor differences between the horizons were analyzed, using optical microscopy, X-ray diffraction (XRD), X-ray fluorescence (XRF), inductively coupled plasma mass spectrometry (ICP-MS), and scanning electron microscope coupled with energy-dispersive X-ray spectroscopy (SEM/EDS).

The mineralogy was determined by XRD on powdered samples (with CoK_{α} radiation and Fe Kβ filter on a Panalytical Empyrean); supported by optical microscopy (with a Leica model DM 2700P) on polished mounts and thin sections — the images used were obtained using gray filter; SEM/EDS (Zeiss LEO 1430 with 500 DP XSD from IXRF-4 Systems Inc) used on small fragments, thin sections and polished mounts, applying secondary and retro-diffused electron detector methods.

The whole-rock chemistry was determined by ALS Ltda. (Belo Horizonte, Brazil) on 20 pulp samples. Major elements were analyzed by XRF, after lithium metaborate or tetraborate fusion (by ME-XRF26 group method); the minor elements by ICP-MS, after digestion by Aqua Regia (ME-MS41), gold determinations by this method are semi-quantitative due to the small sample weight used (0.5g); the rare earth elements (REE) and trace elements were determined by ICP-MS, after lithium borate fusion (ME-MS81U); Cl and F by ion chromatography (Cl-IC881, F-IC881); carbon and total sulfur by Leco furnace and infrared spectroscopy (C-IR07, S-IR08); loss on ignition (LOI) by calcination (OA-GRA05x). The chemical analysis methods used for each element according to the ALS references and respective detection limits are shown in Table 1.

The measured REE contents were normalized to chondrites (Barrat *et al.* 2012). The relative enrichment and depletion of Eu and Ce were evaluated according to the Eu/Eu* and Ce/Ce* ratios (McLennan 1989) defined as: $Eu/Eu^* = Eu_N/(Sm_N \cdot Gd_N)^{0.5}$ and $Ce/Ce^* = 5Ce_N/(4La_N) + (Sm_N)$, where the subscript N denotes the chondrite-normalized value and Eu* represents the Eu value expected for a smooth chondrite-normalized REE pattern. Eu/Eu* values are good indicators of source-rock composition (McLennan 1989).

RESULTS

Mesoscopic classification of the iron ore profile

Typical weathering horizons are displayed in drill hole SSDFD663 (Fig. 3). From the base to the top, they occur respectively as coarse saprolite (459–230 m), fine saprolite (229–31 m), and crust (30 m).

The protore (BIF) shows meso-microbands dominated by magnetite and supergene hematite as accessory mineral phase (Fig. 4A), alternating with quartz/chert, which may contain quartz or carbonate (dolomite) veins with chalcopyrite. At 515 m, a "mafic"-carbonate rock composed of chlorite, biotite, calcite, quartz, magnetite, chalcopyrite, pyrite, hematite, and tourmaline crosscuts the BIF.

The coarse saprolite (CS) horizon is a high-grade hematite ore, soft or powdery (Fig. 4B), commonly showing centimeter-size prism-plates, defined by joint planes and fissile beds, which may display the primary lamination, generally reflecting the original variation in the stratigraphic composition of BIF. Soft ore shows a high amount of hematite, gray color, metallic luster, and high porosity (Fig. 4C), consisting mainly of hematite and minor quartz. Locally, the soft ore contains some manganese oxy-hydroxides ("manganese iron ore," see Fig. 2), as cryptomelane or hollandite. The CS can locally exhibit weathered fragments of fresh BIF, with medium to a low amount of quartz.

The fine saprolite (FS) is the primary domain of soft ore, with fine-grained hematite (> 50 wt.%), and goethite. At the top of FS, a brown and ochreous goethite cement is commonly found filling cavities. A sub-horizon refers to "chemical canga"

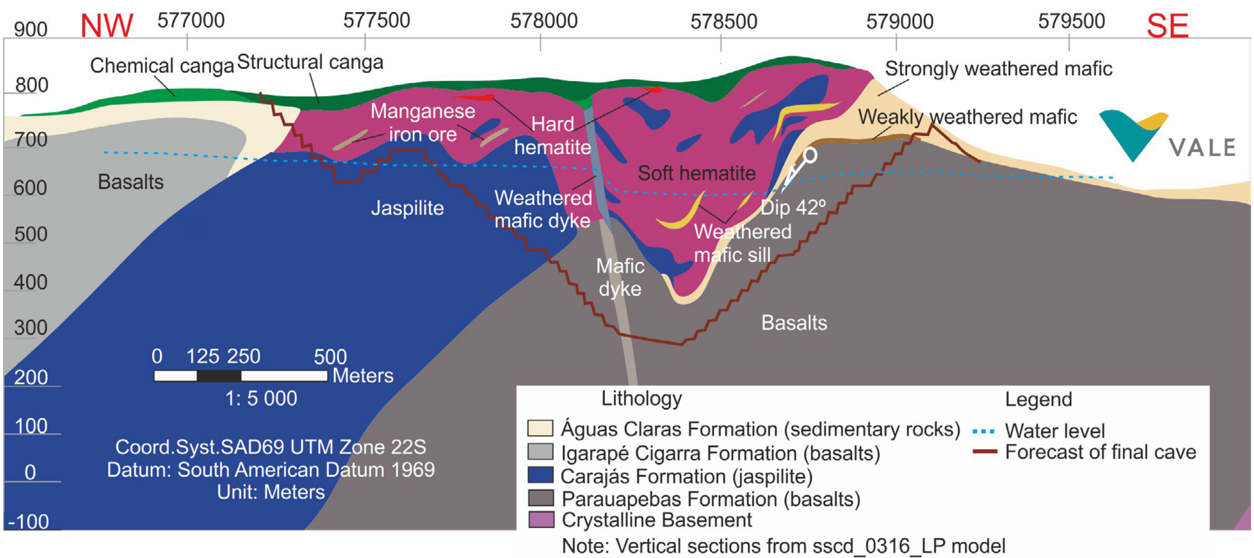

Source: Vale (unpublished data).

Figure 2. The geological cross-section of the S11D mine, with primary lithologies. The terms chemical canga, structural canga, and manganese iron ore, used in the mine geology in Carajás, are explained in the section "Mesoscopic classification of the iron ore profile".

Table 1. Whole-rock major oxide element chemistry of 20 samples from dill hole SSDFD663, at the S11D deposit, Carajás Minaral Province. The major oxide elements are in wt. %, whereas trace elements are in ppm. The numbers in parenthesis indicate the sample's location in meters. The average composition of the upper continental crust (UCC) is after Rudnick & Gao (2003), Chondrites (CH) after Barrat *et al.* (2012) and banded iron formation (BIF) in the Carajás Formation after Macambira & Schrank (2002), Macambira (2003).

			Crust			Fine saprolite			Coarse saprolite						
COMP.	UNIT	DL	AM1 (2)	AM3 (18.3)	AM4 (35)	AM8 (69)	AM13 (110)	AM17 (169)	AM20 (218)	AM22 (255)	AM24 (280)	AM29 (315.3)	AM36 (350)	AM37 (369)	AM45 (410)
SiO_2	%	0.01	1.02	5.66	0.41	0.64	0.99	5.56	47.08	55.88	5.76	39.11	0.55	40.64	3.44
Al_2O_3	%	0.01	1.51	11.26	16.24	3.13	0.75	4.31	0.16	0.31	0.21	0.15	0.09	0.12	0.05
Fe_2O_3	%	0.01	92.23	71.23	64.95	92.47	94.78	79.7	48.22	42.55	93.92	59.96	97.62	58.26	94.76
MnO	%	0.01	0.03	bdl	0.01	bdl	0.02	0.06	2.22	0.03	0.02	0.02	0.65	0.65	0.68
MgO	%	0.01	0.08	bdl	bdl	bdl	0.09	0.09	0.06	0.03	0.06	0.05	0.06	0.07	0.13
CaO	%	0.01	bdl	bdl	bdl	bdl	bdl	bdl	bdl	bdl	bdl	bdl	bdl	bdl	bdl
Na_2O	%	0.01	bdl	bdl	0.01	bdl	bdl	0.06	bdl	0.01	0.01	0.01	0.24	bdl	0.01
K_2O	%	0.01	bdl	0.02	bdl	bdl	bdl	0.01	0.08	0.08	bdl	bdl	0.03	0.02	0.01
BaO	%	0.01	bdl	bdl	bdl	bdl	bdl	bdl	bdl	bdl	bdl	bdl	bdl	bdl	bdl
Cr_2O_3	%	0.01	bdl	0.02	0.03	0.01	bdl	0.01	bdl	bdl	0.01	0.02	bdl	bdl	bdl
TiO_2	%	0.01	0.16	0.94	1.44	0.2	0.06	0.15	bdl	bdl	bdl	bdl	bdl	bdl	bdl
P_2O_5	%	0.01	0.37	0.3	1.68	0.22	0.09	0.22	0.01	0.01	0.01	bdl	0.01	bdl	bdl
SO_3	%	0.01	0.42	0.29	0.39	0.03	0.01	0.03	0.02	bdl	0.04	bdl	0.03	0.02	bdl
SrO	%	0.01	bdl	bdl	0.01	0.01	bdl	0.01	bdl	bdl	0.01	bdl	0.01	0.01	bdl
LOI	%	0.01	4.05	10.13	14.35	3.31	2.92	8.75	0.95	0.59	0.66	0.23	0.67	0.52	0.61
Total	%	0.01	99.92	99.94	99.65	100.10	99.73	99.12	99.08	99.5	100.80	99.58	100.05	100.45	99.80
C	%	0.01	0.21	0.8	0.14	0.05	0.07	0.08	0.07	0.06	0.08	0.04	0.05	0.05	0.06
S	%	0.01	0.01	0.08	0.01	bdl	bdl	bdl	bdl	bdl	bdl	bdl	bdl	bdl	bdl
F	ppm	20	50	80	90	50	50	70	bdl0	bdl0	40	40	bdl0	bdl0	bdl0
Cl	ppm	50	150	80	140	90	120	80	140	110	240	180	140	290	140
Li	ppm	0.1	0.1	0.2	0.1	0.1	0.1	0.2	0.2	0.1	0.2	0.1	0.1	0.2	0.2
Rb*	ppm	0.2	0.2	0.9	bdl	bdl	bdl	0.5	1.4	11.8	0.3	0.2	0.4	0.5	0.3
Cs*	ppm	0.01	0.02	0.08	bdl	bdl	0.01	0.01	0.01	0.08	0.01	0.01	bdl	0.01	0.01
Be	ppm	0.05	0.28	0.13	0.41	0.16	0.36	0.43	0.11	0.13	0.18	0.12	0.12	0.13	0.25
Sr*	ppm	0.1	3.4	5.3	51.3	6	2.2	31.8	10.9	1.4	1.9	1.4	13.9	4	10.5
B	ppm	10	10	10	10	10	10	10	bdl	bdl	bdl	bdl	10	bdl	10
Ge	ppm	0.05	1.91	1.34	0.38	1.39	2.11	1.59	0.38	0.28	1.29	1.96	0.85	0.51	0.86
As	ppm	0.1	1.8	4.2	0.9	0.7	0.8	3	1	1.6	2.4	3.3	1.3	1	1.6
Sb	ppm	0.05	0.18	0.32	0.71	0.41	0.18	0.1	0.07	0.16	0.35	0.08	0.2	0.07	0.22
Te	ppm	0.01	0.03	1.1	0.28	0.04	0.04	0.03	0.03	0.01	bdl	0.02	0.03	0.03	0.02
Sc	ppm	0.1	2.1	4.5	21.4	4.6	1.9	9	0.4	0.7	0.5	0.2	0.2	0.2	0.2
V*	ppm	5	22	173	378	131	17	55	bdl	6	14	bdl	bdl	bdl	17
Cr*	ppm	10	30	130	230	40	20	60	10	30	10	90	bdl	10	bdl
Co*	ppm	0.5	3.2	0.5	1.4	0.7	10.6	15.6	15.2	1.3	5	2.9	13.9	6.8	7.4
Ni	ppm	0.2	1	1.1	3.2	1.8	1.7	8.3	3.9	13.4	4.9	66.7	4.3	7.2	5.2
Cu	ppm	0.2	31.3	14.7	42.5	12.1	66.2	578	590	60.3	18.7	45	172.5	179.5	488
Zn	ppm	2	14	12	13	4	6	26	24	3	7	2	11	8	11
Y*	ppm	0.5	4.7	8.8	22.8	4.8	4.8	15.9	3.3	1.5	2.6	3	3.4	1.4	4.9
Zr*	ppm	2	37	278	357	50	11	30	bdl	5	2	bdl	2	2	bdl
Nb*	ppm	0.2	3.1	16	23.9	3	0.8	1.4	bdl	bdl	bdl	bdl	bdl	bdl	bdl
Mo*	ppm	2	2	3	4	bdl	bdl	2	bdl	bdl	bdl	23	bdl	bdl	3
Ag	ppm	0.01	0.18	0.04	0.02	bdl	0.01	0.02	0.08	0.06	0.05	0.03	0.03	0.11	0.01
Cd	ppm	0.01	0.08	0.02	bdl	bdl	bdl	bdl	0.16	bdl	0.01	bdl	0.05	0.04	0.01
Hf*	ppm	0.2	1.1	7.6	10	1.6	0.3	0.8	bdl	bdl	bdl	bdl	bdl	bdl	bdl
Ta*	ppm	0.1	0.2	1.2	1.7	0.2	0.1	0.1	bdl	bdl	bdl	bdl	bdl	bdl	bdl

Continue...

Table 1. Continuation.

			Crust			Fine saprolite			Coarse saprolite						
COMP.	UNIT	DL	AM1 (2)	AM3 (18.3)	AM4 (35)	AM8 (69)	AM13 (110)	AM17 (169)	AM20 (218)	AM22 (255)	AM24 (280)	AM29 (315.3)	AM36 (350)	AM37 (369)	AM45 (410)
W*	ppm	1	11	5	13	2	2	3	2	4	7	2	4	2	3
Re	ppm	0.001	0.001	bdl	0.001	0.001	bdl	0.001	bdl	0.001	0.001	0.001	bdl	bdl	bdl
Au	ppm	0.02	bdl	bdl	bdl	bdl	bdl	bdl	bdl	bdl	bdl	bdl	bdl	bdl	bdl
Hg	ppm	0.01	0.18	0.28	0.06	0.02	0.02	0.03	0.02	0.02	0.02	0.02	0.01	0.02	bdl
Th*	ppm	0.05	3.14	12.45	26.8	4.28	1.04	1.87	bdl	0.31	0.06	bdl	0.07	bdl	0.05
U*	ppm	0.05	1.1	2.15	4.3	1.06	5.93	3.44	0.18	1.41	0.89	1.16	0.29	0.17	2.51
Ga*	ppm	0.1	4.3	20.6	47.1	6.4	2.4	6.9	0.9	1.1	0.3	0.3	0.4	0.4	0.5
In	ppm	0.005	0.026	0.08	0.19	0.034	0.008	0.026	bdl	0.008	0.005	bdl	0.011	0.006	0.015
Tl*	ppm	0.5	bdl	bdl	bdl	bdl	bdl	bdl	bdl	bdl	bdl	bdl	bdl	bdl	bdl
Pb	ppm	0.2	1.9	10.7	1.2	0.5	0.7	2.8	1.3	0.6	1.8	0.7	1.3	1.4	2.5
Sn*	ppm	1	1	3	7	1	1	1	bdl	1	1	bdl	bdl	bdl	bdl
Bi	ppm	0.01	0.09	0.43	0.17	0.13	0.05	0.13	0.06	0.04	0.09	0.03	0.07	0.07	0.15
Se	ppm	0.2	bdl	0.9	bdl	bdl	bdl	bdl	bdl	bdl	bdl	bdl	bdl	bdl	bdl
La*	ppm	0.5	6.6	6.1	37.1	2.8	4.3	38.5	9.8	2.6	2.1	4	4	4.9	5.4
Ce*	ppm	0.5	8.2	10.3	74.1	10.3	9.5	42.6	6.4	4.6	2.8	4.5	4.6	4.1	5.2
Pr*	ppm	0.03	1.07	1.06	6.9	0.6	0.9	9.44	1.91	0.39	0.38	0.43	0.5	0.71	0.91
Nd*	ppm	0.1	3.3	3.4	22.5	2	3	32.2	7	1.2	1.4	1.1	1.8	2.5	3.9
Sm*	ppm	0.03	0.67	0.75	4.07	0.48	0.64	7.79	1.67	0.22	0.31	0.1	0.42	0.57	1.1
Eu*	ppm	0.1	0.22	0.19	1.02	0.17	0.24	2.89	0.68	0.09	0.17	0.11	0.25	0.25	0.49
Gd*	ppm	0.05	0.48	0.85	3.4	0.51	0.48	5.67	1.17	0.2	0.26	0.12	0.38	0.39	0.86
Tb*	ppm	0.01	0.08	0.18	0.6	0.09	0.08	0.93	0.18	0.03	0.04	0.02	0.05	0.06	0.14
Dy*	ppm	0.05	0.53	1.33	3.88	0.6	0.47	5.44	0.91	0.2	0.28	0.12	0.33	0.3	0.73
Ho*	ppm	0.01	0.11	0.29	0.81	0.15	0.11	1.01	0.15	0.05	0.05	0.03	0.06	0.05	0.13
Er*	ppm	0.03	0.35	1	2.38	0.45	0.35	2.73	0.36	0.12	0.16	0.13	0.2	0.14	0.36
Tm*	ppm	0.01	0.05	0.17	0.54	0.08	0.06	0.4	0.05	0.02	0.02	0.01	0.03	0.02	0.04
Yb*	ppm	0.03	0.38	1.21	2.31	0.56	0.37	2.62	0.32	0.13	0.12	0.1	0.16	0.11	0.23
Lu*	ppm	0.01	0.07	0.19	0.34	0.08	0.06	0.38	0.04	0.02	0.01	0.02	0.02	0.02	0.03
Eu/Eu*	ppm		1.19	0.73	0.84	1.05	1.32	1.33	1.49	1.31	1.83	3.07	1.91	1.62	1.54
Ce/Ce*	ppm		0.57	0.77	0.92	1.65	1.00	0.49	0.29	0.82	0.60	0.53	0.53	0.38	0.43
ΣLREE			20.54	22.65	149.1	16.86	19.06	139.1	28.63	9.3	7.42	10.36	11.95	13.42	17.86
ΣHREE			1.57	4.37	10.86	2.01	1.5	13.51	2.01	0.57	0.68	0.43	0.85	0.7	1.66
ΣREE			22.11	27.02	160	18.87	20.56	152.6	30.64	9.87	8.1	10.79	12.8	14.12	19.52

			Coarse Saprolite				Protore						
COMP.	UNIT	DL	AM46 (434)	AM47 (455)	AM49b (466.5)	AM51 (476.5)	AM52 (490)	AM54 (522)	AM55 (524.5)	UCC	CH	BIF	Factor Min./Max.
SiO_2	%	0.01	0.48	0.5	4.61	0.48	42.82	45.99	50.39	66.6		44.6	0.01/0.84
Al_2O_3	%	0.01	0.21	0.14	0.32	0.21	0.33	1.16	0.26	15.4		0.63	0.00/1.05
Fe_2O_3	%	0.01	94.97	89.39	69.36	68.15	57.68	35.93	44.59	5.04		53.65	7.13/19.37
MnO	%	0.01	2.96	5.28	13.35	23.7	0.02	0.57	0.1	0.10		0.06	0.10/237.00
MgO	%	0.01	0.05	0.05	0.02	0.06	0.05	4.62	1.29	2.48		0.1	0.01/1.86
CaO	%	0.01	bdl	0.01	0.08	0.05	bdl	0.08	1.86	3.59		0.04	0.00/0.52
Na_2O	%	0.01	bdl	bdl	bdl	bdl	bdl	0.01	bdl	3.27		0.04	0.00/0.07
K_2O	%	0.01	0.18	0.12	0.29	1.18	bdl	0.05	bdl	2.80		0.04	0.00/0.42
BaO	%	0.01	bdl	0.52	1.32	0.29	bdl	bdl	bdl				/
Cr_2O_3	%	0.01	bdl	0.01	0.01	bdl	bdl	bdl	bdl				/
TiO_2	%	0.01	bdl	bdl	bdl	bdl	bdl	0.04	bdl	0.64		0.02	0.06/2.25
P_2O_5	%	0.01	0.01	0.09	0.39	0.02	0.01	0.02	0.01	0.15		0.01	0.07/11.20

Continue...

Table 1. Continuation.

			Coarse Saprolite				Protore						
COMP.	UNIT	DL	AM46 (434)	AM47 (455)	AM49b (466.5)	AM51 (476.5)	AM52 (490)	AM54 (522)	AM55 (524.5)	UCC	CH	BIF	Factor Min./Max.
SO_3	%	0.01	0.03	bdl	0.04	0.03	0.02	0.52	0.2				/
SrO	%	0.01	0.01	0.01	0.04	0.04	0.01	bdl	0.01				/
LOI	%	0.01	0.86	4.24	8.57	4.14	-0.13	11.4	1.51			0.73	/
Total	%	0.01	100.05	100.85	99.86	100.5	100.85	100.55	100.25	100.05		-	0.99/1.01
C	%	0.01	0.06	0.04	0.08	0.05	0.06	3.39	0.81				/
S	%	0.01	bdl	bdl	bdl	bdl	bdl	0.23	0.08	0.062			0.16/3.70
F	ppm	20	bdl	20	bdl	bdl	bdl	120	60	557			0.04/0.22
Cl	ppm	50	190	100	60	110	bdl	700	100	294			0.20/2.38
Li	ppm	0.1	0.2	0.3	0.1	0.2	0.2	0.2	0.2	24	1.44		0.00/0.01
Rb*	ppm	0.2	4.5	2.7	8.1	27.7	0.3	2.8	0.5	82	2.33		0.00/0.34
Cs*	ppm	0.01	0.04	0.04	0.12	0.12	0.04	0.16	0.04	4.9	0.189		0.00/0.03
Be	ppm	0.05	0.27	0.43	2.42	1.04	0.08	0.11	0.35	2.1	0.023		0.04/1.15
Sr*	ppm	0.1	53.7	41.7	345	273	0.9	5.2	4.9	320	7.74		0.00/1.08
B	ppm	10	10	10	bdl	bdl	10	10	10	17			0.59/0.59
Ge	ppm	0.05	1.09	1.35	1.93	0.84	0.9	1.23	0.93	1.4			0.20/1.51
As	ppm	0.1	1.8	3.9	100.5	3.8	1.9	3.7	2.3	4.8			0.15/20.94
Sb	ppm	0.05	0.22	0.07	0.17	0.2	0.2	0.06	0.2	0.4		7.43	0.15/1.78
Te	ppm	0.01	bdl	0.03	0.02	bdl	0.02	0.07	0.03				/
Sc	ppm	0.1	0.3	0.3	0.9	0.5	0.2	1.1	0.3	14.0	5.85	0.27	0.01/1.53
V*	ppm	5	bdl	5	13	57	bdl	7	bdl	97	52.4		0.05/3.90
Cr*	ppm	10	bdl	20	110	10	10	130	110	92	2627		0.11/2.50
Co*	ppm	0.5	15.1	32.3	208	149.5	1.5	4.6	8.1	17.3	520		0.03/12.02
Ni	ppm	0.2	1.3	12.1	51.3	4.3	0.9	42.6	67.2	47	11300	7.85	0.02/1.43
Cu	ppm	0.2	172.5	278	2250	1955	59.8	373	66.1	28	127	29.79	0.43/80.4
Zn	ppm	2	40	68	228	197	8	15	8	67	303	66.58	0.03/3.40
Y*	ppm	0.5	5.8	5.6	38	18.4	1.2	2.6	4.5	21	1.56		0.06/1.81
Zr*	ppm	2	2	bdl	bdl	bdl	bdl	24	2	193	3.52	16.89	0.01/1.85
Nb*	ppm	0.2	bdl	bdl	bdl	bdl	bdl	0.7	bdl	12	0.289		0.06/1.99
Mo*	ppm	2	bdl	bdl	5	bdl	bdl	2	2	1.1			1.82/20.91
Ag	ppm	0.01	0.01	0.04	1.54	0.29	0.02	0.08	0.05	53			0.00/0.03
Cd	ppm	0.01	0.01	0.18	0.5	1.32	bdl	0.01	0.01	0.09			0.11/14.67
Hf*	ppm	0.2	bdl	bdl	bdl	bdl	bdl	0.7	bdl	5.3	0.107		0.06/1.89
Ta*	ppm	0.1	bdl	bdl	bdl	bdl	bdl	0.1	bdl	0.9	0.015		0.11/1.89
W*	ppm	1	3	2	1	1	1	1	1	1.9	0.11		0.53/6.84
Re	ppm	0.001	0.001	0.001	bdl	bdl	bdl	0.002	bdl	0.198			0.01/0.01
Au	ppm	0.02	bdl	bdl	0.04	0.04	0.03	0.03	0.03	1.5			0.02/0.03
Hg	ppm	0.01	0.01	0.05	0.46	0.08	bdl	0.01	bdl	0.05			0.20/9.20
Th*	ppm	0.05	0.17	bdl	bdl	bdl	bdl	1.69	0.23	10.5	0.028		0.00/2.55
U*	ppm	0.05	1.91	0.67	1.96	2.34	0.28	0.58	0.34	2.7	0.008		0.06/2.20
Ga*	ppm	0.1	1	2.5	7.3	10.8	0.4	1.6	0.9	17.5	9.48		0.02/2.69
In	ppm	0.005	0.033	0.006	bdl	0.037	0.008	0.042	0.015	0.056			0.09/3.39
Tl*	ppm	0.5	bdl	5.7	11.6	1.1	bdl	bdl	bdl	0.9			1.22/12.89
Pb	ppm	0.2	2.4	2	2	5.2	0.6	1.1	0.7	17	2.69	18.33	0.03/0.63
Sn*	ppm	1	bdl	bdl	bdl	bdl	bdl	1	bdl	2.1			0.48/3.33
Bi	ppm	0.01	0.11	0.05	0.02	0.13	0.01	0.37	0.17	0.16		6.2	0.06/2.69
Se	ppm	0.2	bdl	bdl	0.4	0.8	bdl	0.4	bdl	0.09			4.44/10.00
La*	ppm	0.5	4.9	5.9	46.4	46.6	1.1	2.3	7.1	31	0.235		0.04/1.50

Continue...

Table 1. Continuation.

			Coarse Saprolite				Protore						
COMP.	**UNIT**	**DL**	**AM46 (434)**	**AM47 (455)**	**AM49b (466.5)**	**AM51 (476.5)**	**AM52 (490)**	**AM54 (522)**	**AM55 (524.5)**	**UCC**	**CH**	**BIF**	**Factor Min./Max.**
Ce*	ppm	0.5	5.9	4.6	13.3	6.1	1.4	3.7	11.4	63	0.6	2.38	0.02/1.18
Pr*	ppm	0.03	0.93	0.73	9.69	11.35	0.16	0.41	1.25	7.1	0.091		0.02/1.60
Nd*	ppm	0.1	3.7	3.2	40.6	47.6	0.6	1.6	4.2	27	0.464	1.9	0.02/1.76
Sm*	ppm	0.03	0.87	0.86	8.43	13.2	0.11	0.29	0.69	4.7	0.153	0.25	0.02/2.81
Eu*	ppm	0.1	0.48	0.28	3.62	5.52	0.07	0.09	0.2	1.0	0.059	0.17	0.07/5.52
Gd*	ppm	0.05	1.25	0.68	8.67	9.49	0.1	0.29	0.59	4.0	0.206	0.25	0.03/2.37
Tb*	ppm	0.01	0.19	0.12	1.08	1.24	0.01	0.03	0.08	0.7	0.038		0.01/1.77
Dy*	ppm	0.05	1.12	0.71	5.49	5.2	0.06	0.25	0.5	3.9	0.254		0.02/1.41
Ho*	ppm	0.01	0.2	0.15	0.97	0.78	0.01	0.06	0.1	0.83	0.057		0.01/1.22
Er*	ppm	0.03	0.5	0.45	2.59	1.85	0.04	0.25	0.29	2.3	0.166		0.02/1.19
Tm*	ppm	0.01	0.05	0.04	0.35	0.27	bdl	0.04	0.04	0.30	0.026		0.03/1.80
Yb*	ppm	0.03	0.35	0.31	2	1.51	0.04	0.24	0.26	2.0	0.168	0.15	0.02/1.31
Lu*	ppm	0.01	0.04	0.05	0.3	0.22	0.01	0.03	0.03	0.31	0.025	0.02	0.03/1.23
Eu/Eu*	ppm		1.41	1.12	1.29	1.51	2.04	0.95	0.96				
Ce/Ce*	ppm		0.54	0.35	0.13	0.06	0.59	0.73	0.74				
ΣLREE			18.03	16.25	130.7	139.9	3.54	8.68	25.43				
ΣHREE			2.45	1.83	12.78	11.07	0.17	0.9	1.3				
ΣREE			20.48	18.08	143.5	150.9	3.71	9.58	26.73			5.27	

*Elements determined by ME-MS81U method used in figures 9 to 13; DL: detection limit; LOI: loss on ignition; bdl: below detection limit.

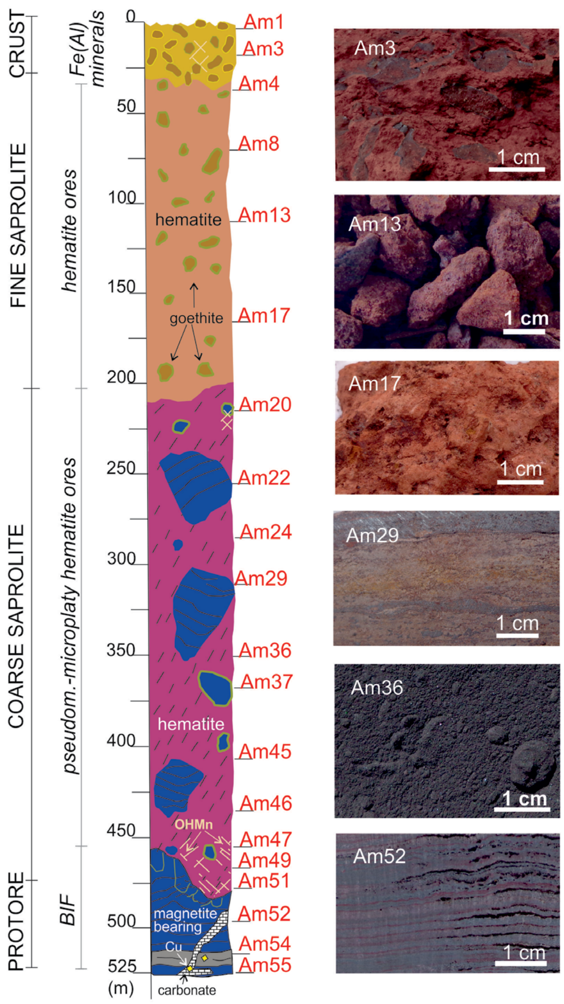

Figure 3. Simplified lateritic weathering profile and location of 20 samples collected from the S11D mine.

(Fig. 2), consists of ochreous goethite, kaolinite, and gibbsite, which have a clay particle size (Fig. 4D).

The iron-crust at the top of the profile is called "structural canga" (up to 30 m thick, see Fig. 2), is coarse-grained (Fig. 4E), stratified and highly porous. It is composed of coarse-grained to massive hematite, with ochreous and brown goethite cement.

Microtextures related to the iron ore profile

Iron minerals at the protore consist of 90% of euhedral magnetite crystals (mt, Figs. 5A and 5B) and 10% of micro-platy hematite (mpl, Fig. 5C). The magnetite bands are mostly massive and horizontally continuous (Fig. 5A) in macro and microscale. However, at its boundaries large, octahedral magnetite crystals (< 100 μm) are displayed, in contact with quartz bands (Fig. 5B). The majority of the microplaty hematite (1–10 μm) is also disseminated within quartz bands (Fig. 5C).

Near the weathering front, the magnetite crystals present pseudomorph substitution by hematite (psh), located from the edges toward the centers (Fig. 5D). In addition, there is an increase of porosity with the dissolution of the quartz/chert (Fig. 5E), causing the collapse of the iron bands (Fig. 5F).

At the saprolite, the fragments of collapsed iron bands are dominant and composed of hematite pseudomorphs after magnetite with high interparticle and intraparticle porosity. Interparticle occurs as spherical (Fig. 6A) to large elongated cavities (Fig. 6B). Although intraparticle occurs in the pseudomorph hematite crystals, they show sharp, rounded, and wave edges (Figs. 6C and 6D). The studies of Varajão *et al.* (1996) and Taylor *et al.* (2001) showed that the loss of rock volume due to dissolution may reach up to 40%. Primary microplaty hematite (Figs. 6E and 6F) shows no evidence of modification by weathering along the S11D profile, because hematite is stable in many environmental conditions (Das *et al.* 2011).

At the top of the profile, goethite occurs as a cement between the fragments of iron bands (Fig. 7). There are many generations of goethite cement, forming concentric layers from the cavities wall towards the center (Fig. 7A). The habit of goethite ranges from fibrous, acicular to rods crystals (Fig. 7B). Also, some of the pseudomorph hematite crystals are filled by

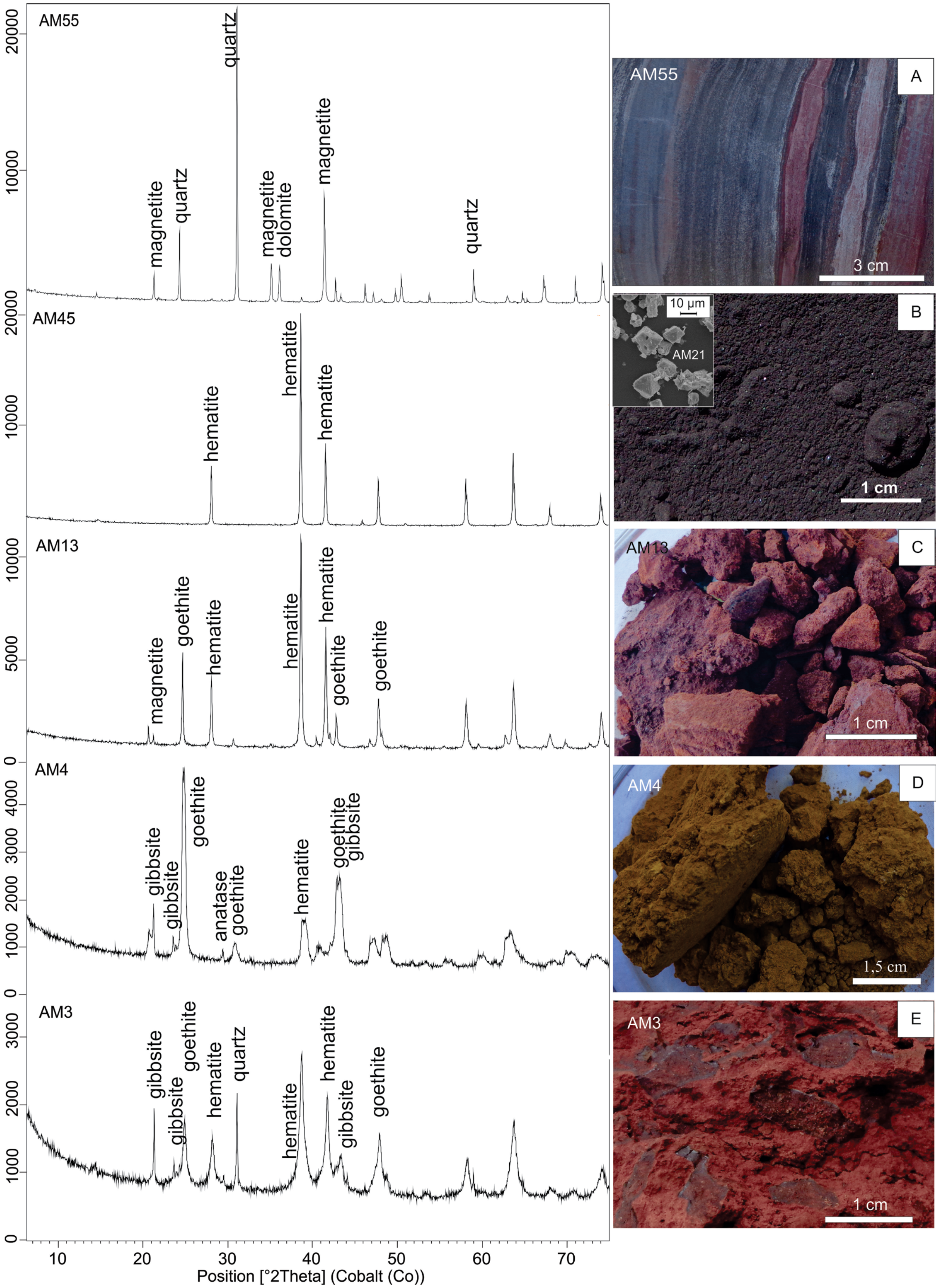

Figure 4. Mineralogy identified by X-ray diffraction (XRD) from samples collected from the S11D mine. (A) Banded iron formation (BIF), black bands composed of hematite and magnetite, and light bands of jasper or chert; (B) soft hematite, the main composition is hematite (scanning electron microscope micrography); (C) hematite ore; (D) ochreous goethite, probably aluminum-bearing; (E) brown goethite, iron crust.

goethite, *i.e.*, ghost-crystals, preserving only the old hematite borders (Fig. 7C). Microanalysis of the different generations of goethite (Fig. 7D) developed in the cavities has shown minor amount of Al_2O_3 and SiO_2.

Whole-rock chemistry

Major oxides and trace elements

The 20 analyzed samples of S11D (Tab. 1) are composed of the same three major oxides and LOI that are shown by the box and whisker plot (Fig. 8). The sum of Fe_2O_3 and SiO_2 make up to 70% of the whole-rock chemistry for most of the samples (Tab. 1). The total iron oxide content is ranging from 42.55 to 97.62 wt.% Fe_2O_3 (with a median of 69 wt.%) (Fig. 8). The SiO_2 in the full profile ranges from 0.10 to 56.17 wt.% (Fig. 8). Indeed, SiO_2 and Fe_2O_3 are strongly negatively correlated (Fig. 9 and Fig. 10A), what is compatible with a lateritic evolution (Costa 1991). Besides Fe_2O_3, only three major chemical components are exhibited higher than 10 wt.% in the samples: Al_2O_3 (up to 16.24%), MnO (up to 23.70%) and LOI (up to 14.35%). However, more than 75% of the samples show less than 1.0 wt.% Al_2O_3 (Fig. 8).

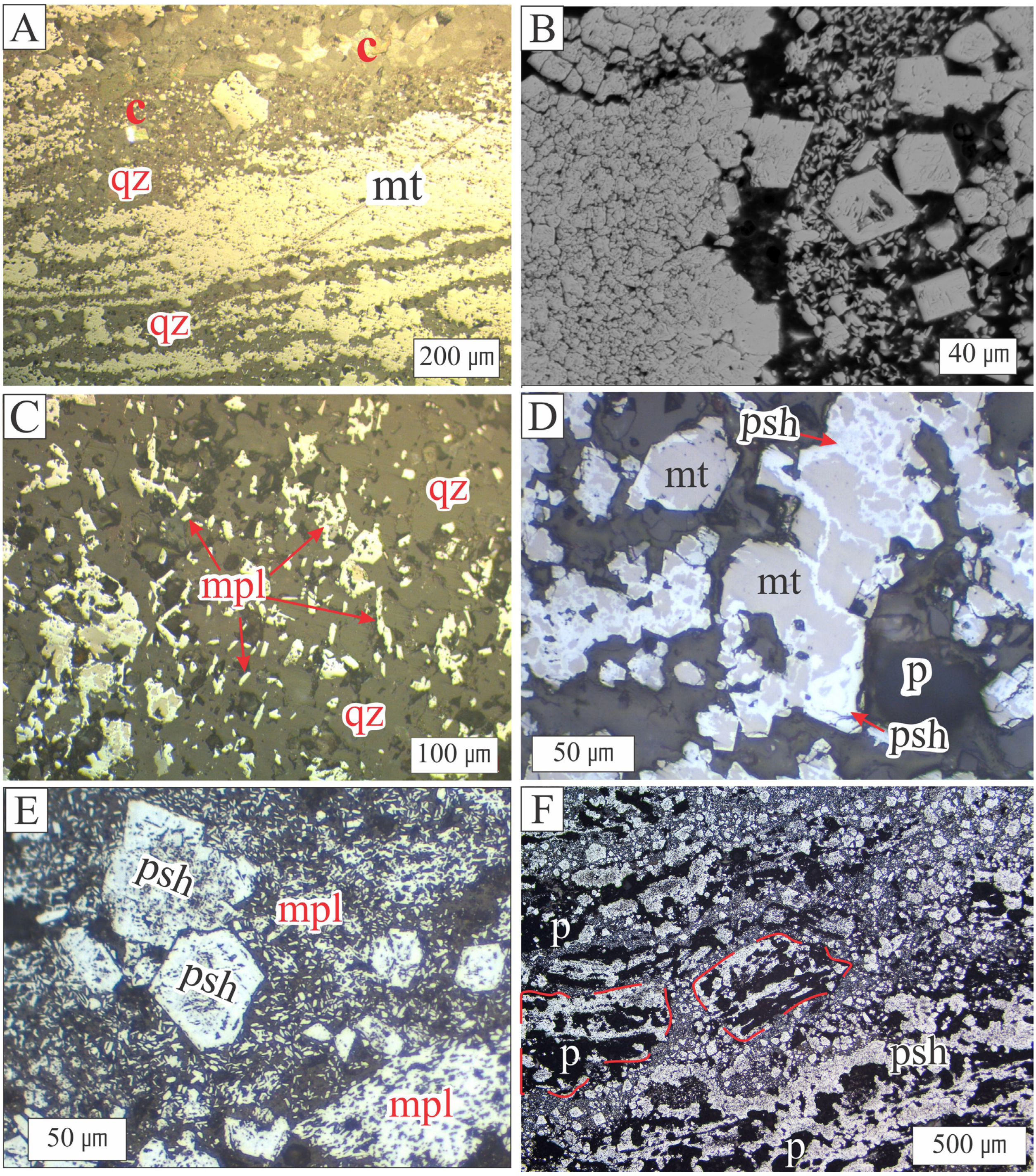

Figure 5. Mineralogy of the lateritic profile in the S11D samples. (A) Bands of magnetite (mt), quartz (qz), and carbonate (c). (B) Massive magnetite bands (left-hand-side), euhedral crystals of mt and microplaty hematite (right-hand-side) (white) (mpl). (C) Microplaty hematite (white) (mpl) and quartz (dark grey). (D, E) Hematite pseudomorph after magnetite (psh). (F) Fragments of collapsed iron bands. Photomicrographs under reflected light (A, C, D, E, F) and scanning electron microscope by retro-diffused electron (B); micropores (p) are black.

The TiO_2 and P_2O_5 are very low (< 0.02 wt.%) at the protore and coarse saprolite (Tab. 1). On the other hand, samples of fine saprolite and crust behave enriched (Tab. 1) when compared with the average of the upper continental crust (UCC, Fig. 11). The Al_2O_3 shows a good positive correlation (r = 0.85) with P_2O_5 (Fig. 10B) and (r = 0.99) TiO_2 (Fig. 10C). Probably, P_2O_5 occurs as aluminum phosphate, a common situation in laterite profiles (Costa 1991).

The percentage of the alkali and alkali earth metals is less than 1.0 wt.% in most of the samples (Tab. 1). At the bottom of the profile > 1 wt.% of major oxide elements, can be found, for example, MgO ranges from 0.05 to 4.62 wt.%, CaO from 0.08 to 1.86 wt.%, and K_2O from 0.01 to 1.18 wt.%. These chemical aspects are typical of laterite profile evolution (Costa 1991). The MgO and CaO are negatively correlated, which corresponds with the replacement of calcite by dolomite. The MnO and K_2O show positive correlation (r = 0.95) locally (Fig. 10D), which correspond to manganese oxides, such as cryptomelane and hollandite, identified as occasional mineral in the profile and can be of lateritic origin (Requelme 2013, Costa 2015). The highest MnO content (up to 24.19% MnO — median 0.6 wt.%) has been observed at the bottom of the coarse saprolite.

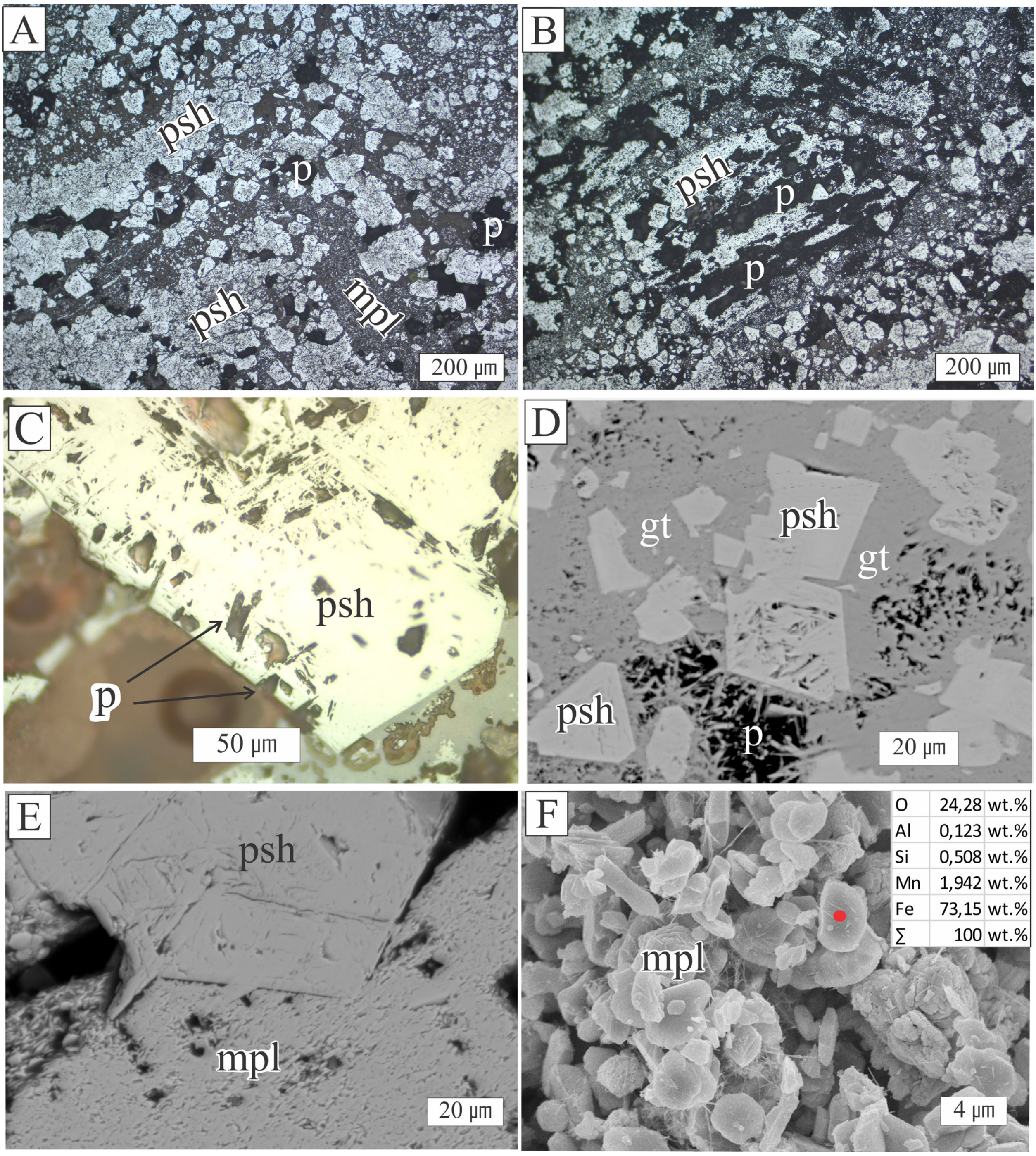

O	24,28	wt.%
Al	0,123	wt.%
Si	0,508	wt.%
Mn	1,942	wt.%
Fe	73,15	wt.%
∑	100	wt.%

Figure 6. Iron oxide dissolution and fracture textures. (A, B) Banded iron formation (BIF), euhedral light-colored crystals of hematite pseudomorphs after magnetite (psh); (C, D) "psh" showing intraparticle porosity; (E) relationship between "psh" and "mpl"; (F) "mpl" with some contaminants (cryptomelane-hollandite???). (A, B, C) Photomicrographs under reflected light, (D, E) scanning electron microscope (SEM) by retro-diffused electron, and (F) SEM by secondary electron. Microporosity (p) is shown as black areas. The red point indicates the position of the microanalysis, whose results are indicated at the top right of the image.

The trace elements content is variable along the horizons of the investigated profile (Fig. 9). Two groups of elements have been identified after content distribution and enrichment factor, when compared with the UCC (Tab. 1). The first group comprises Co, Ni, Cu, Zn, Y, and Cd, which are concentrated mainly in the protore and coarse saprolite horizon, whereas the second one, Sc, V, Cr, Zr, Nb, Mo, Hf, Ta, W, Th, U, and Hg, are concentrated in the fine saprolite and crust (Figs. 9 and 11B). Most of the transition metals display a positive correlation with Al_2O_3-TiO_2-P_2O_5, and between each other, as shown in Figures 10E and 10F.

Other trace elements concentrated at the bottom of the coarse saprolite (AM49B) are Be, Sr, Ba, As, Ta (Fig. 11A). C, S, F, and Cl, mainly related to the mafic-carbonate rock, exceeding the values of concentration for the UCC with the maximum factor of enrichment of 3 (Tab. 1).

At the top of the profile, trace elements such as Ga, In, Pb, Sn, Bi, and Se exhibit relative high concentrations (Tab. 1). Those elements show a positive correlation with Al_2O_3-TiO_2-P_2O_5 (Fig. 9). The trace elements Ga, Pb, Bi, Co, Ni, and Zn display an enrichment in the fine grained saprolite and crust (Fig. 12A and B).

Chondrite-normalized REE trends of these rocks showed that the light rare earth element- (LREE) are enriched (> 1) and heavy rare earth element (HREE) are depleted (< 1), with pronounced positive Eu- (median = 1.31) and negative Ce anomalies (median = 0.57) (Tab. 1). A minor depletion of Eu can be observed in samples 3, 4, 54, and 55, whereas sample 13 shows enrichment in Ce (Fig. 13A). The lanthanoids display a higher concentration of LREE in the coarse saprolite, whereas the HREE are more concentrated in the

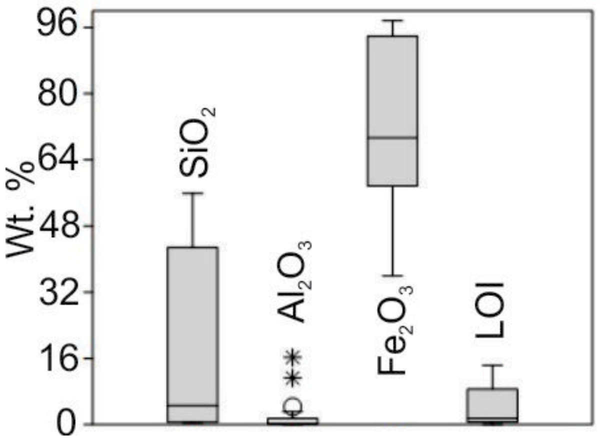

Figure 8. Box and whisker plot for the four major oxide components of the 20 samples from the S11D mine. The black horizontal line represents the median.

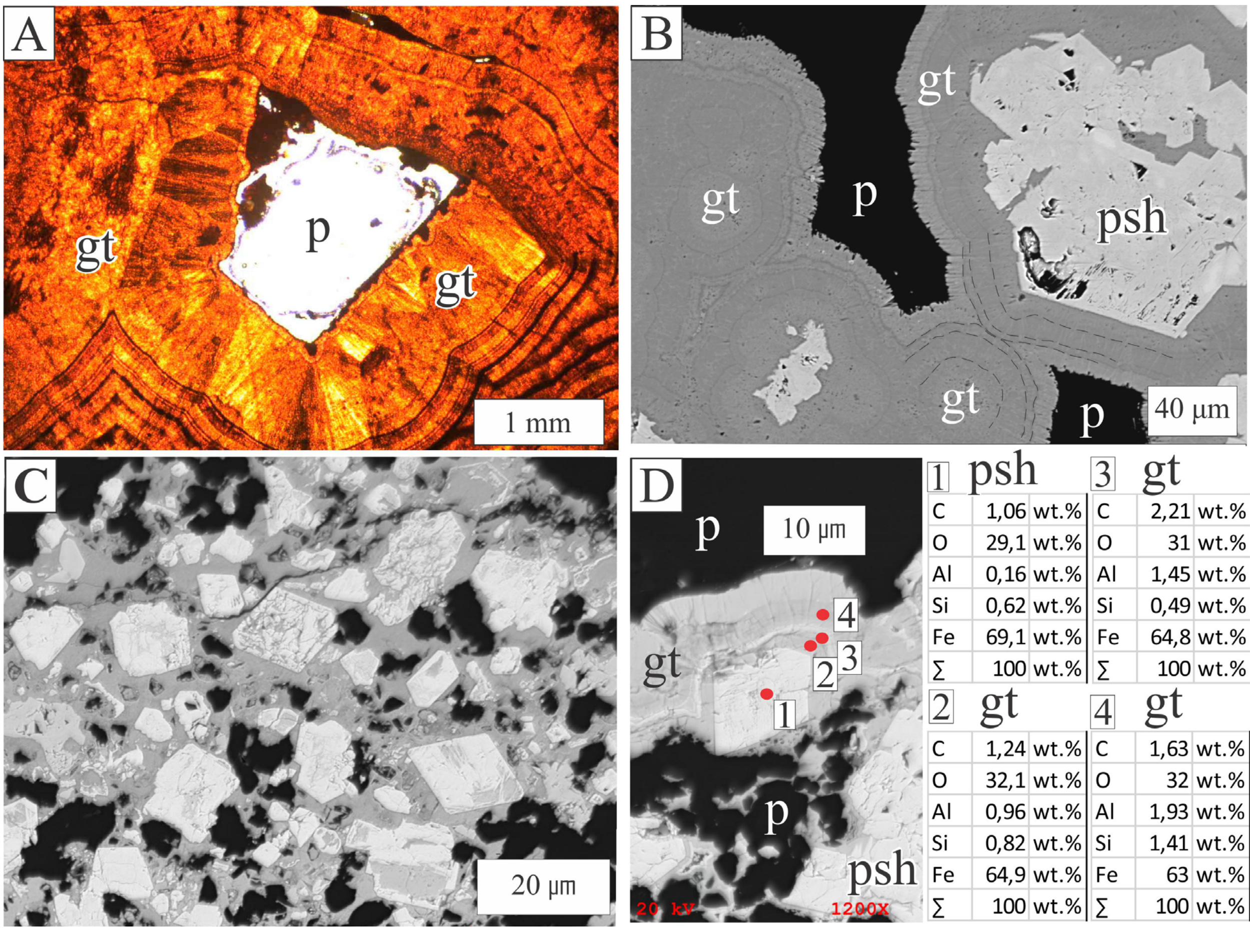

Figure 7. Iron oxides cementation textures. (A) Concentric fibrous banding of goethite (gt); the banding is concentric towards the porosity center; (B) concentric fibrous, acicular to bands of goethite; (C) hematite pseudomorph after magnetite (psh) exhibit corroded boundaries and sharp to rounded edges; goethite cement has filled the "ghost" crystals; most pseudomorph hematite crystals dissolved along preferential crystal faces; (D) microanalyses demonstrate variation in the composition of goethite layers, with the most enriched being Fe, Al and Si. (A) Photomicrographs under plane-polarized light and (B, C, D) scanning electron microscope by retro-diffused electron. Microporosity (p) is shown as black areas. Red points (1–4) at image D indicate the position of the microanalyses, whose results are shown at the right of this image.

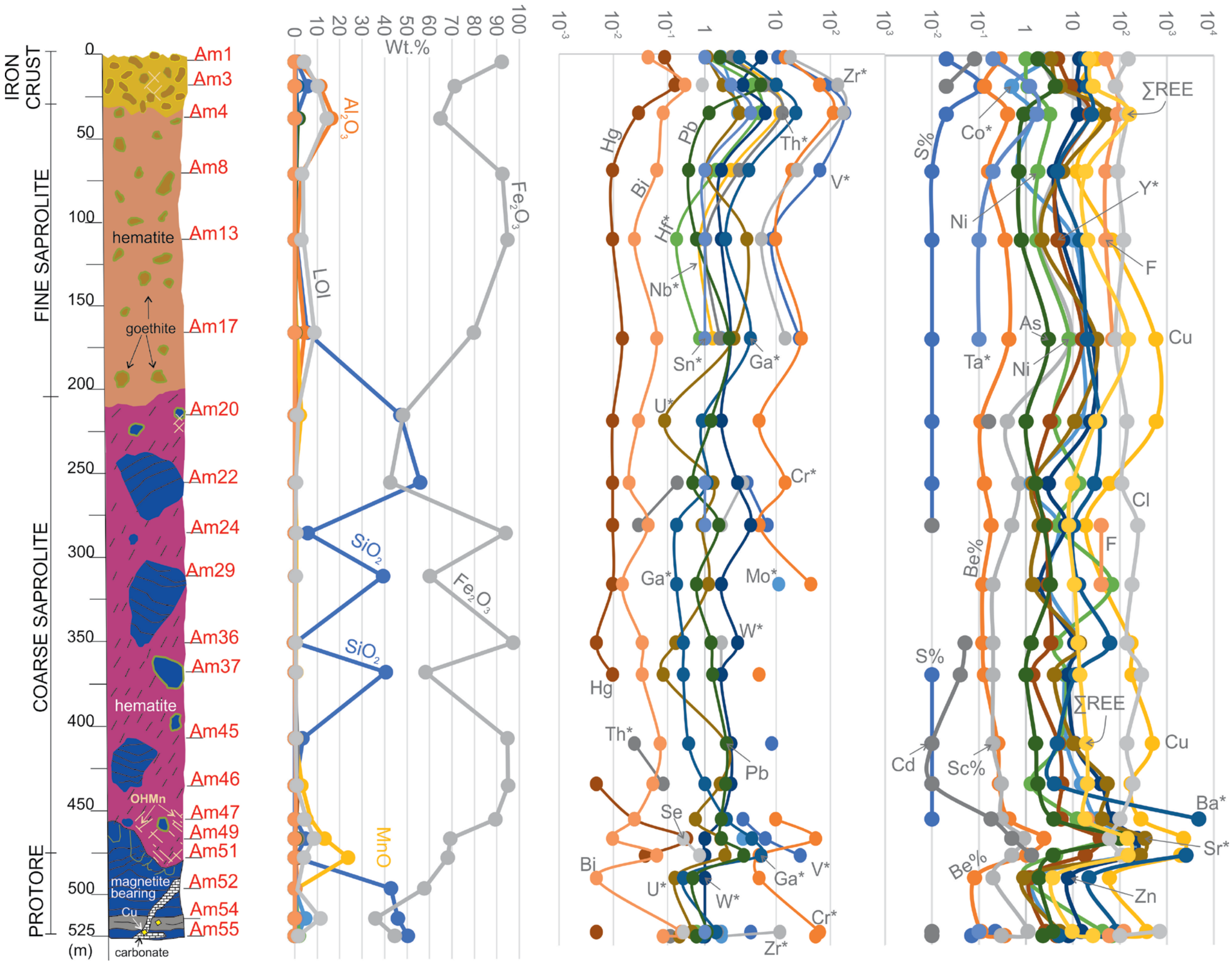

Figure 9. Chemostratigraphy of major oxide elements and trace elements of 20 samples from the S11D deposit. Discontinuous lines represent values that are below the detection limit.

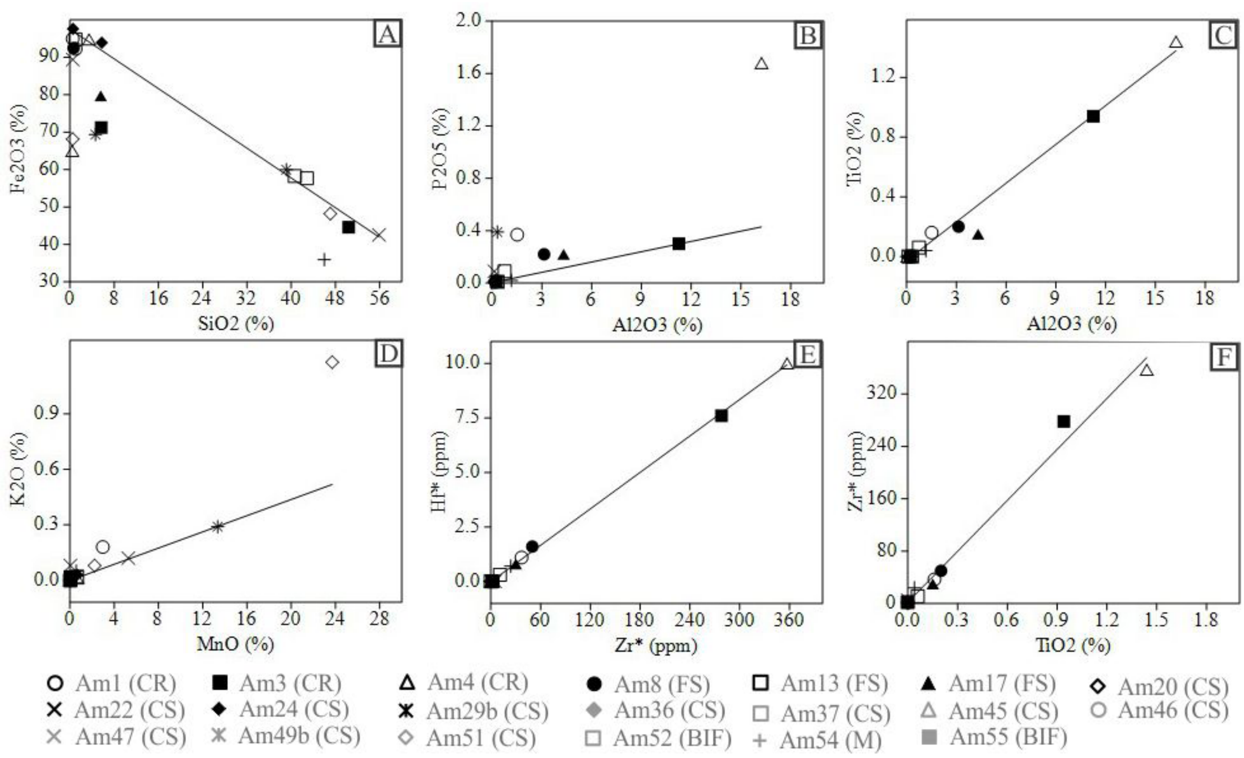

CR: crust; FS: fine saprolite; CS: coarse saprolite; M: mafic rock; *see Table 1.

Figure 10. Bivariate major oxide plots of samples from the S11D deposit: (A) $Fe_2O_3 \times SiO_2$; (B) $P_2O_5 \times Al_2O_3$; (C) $TiO_2 \times Al_2O_3$; (D) $K_2O \times MnO$; (E) Hf × Zr; (F) Zr × TiO_2.

crust (Fig. 13B). The most significant Eu anomalies are in the saprolite samples, with a maximum of 3.07 ppm (Tab. 1).

DISCUSSION

From the mineralogical point of view, this study has shown that different stages of oxidation have occurred along the profile. In the coarse saprolite, octahedral magnetite was replaced by hematite. Craig and Vaughan (1981) showed that the planes (111) control the substitution in both iron oxides, resulting in hematite pseudomorphs after magnetite (Fig. 5). This process commonly takes place from the edges towards the center of the crystals, being generally known as "martitization" (Davis *et al*. 1968, Varajão *et al*. 1996). The substitution can be easily identified during its early stage because of the large amount of magnetite remaining in the center of the crystals (Fig. 5D). More advanced stages occur in the coarse saprolite, where magnetite may be reduced to "islands". Complete replacement of magnetite is often difficult to distinguish at the FS and crusts unless vestigial structures, such as the typical octahedral crystal morphology (Fig. 5E), is still visible.

The dissolution of fine-grained quartz and chert by weathering is one of the main processes occurring in this profile. The extensive dissolution of quartz, carbonate, and manganese hydroxide has formed spherical to elongated, up to centimeter-long cavities (Fig. 5F), reaching from the coarse saprolite into the iron ores. In addition, the original band in the BIF is preserved up to the top part of the profile, as shown by Costa and Araújo (1997) and Costa *et al*. (2011), even if the opaque iron oxide bands are fractured and collapsed.

According to White and Buss (2014) and Zhu *et al*. (2017), the dissolution of quartz and chert is a slow chemical process, via adsorption of water molecules on the surface of these minerals, resulting in further formation of four silanol groups around the silicon atom and the detachment of the molecules of orthosilicic acid from the surface. Sokolova (2013) explained that during the final stage of the hydrolysis reaction there is a release of Si atoms that are surrounded by four OH groups (*i.e.*, the orthosilicic acid H_4SiO_4) into the solution, with the rates of quartz dissolution at pH 7 and 3 are $10^{-15.72}$ and $10^{-16.12}$ mol/m^2 s, respectively.

The goethite texture ranges from firmly indurated brown material to very friable yellow ochre. The botryoidal goethite is formed by concentric layers of radial acicular crystals, which may have termination suggestive of rhombohedral or rhombic forms (Figs. 7A and 7B), usually deposited as a dark brown film on the walls of cavities. Tardy and Nahon (1985) studied the formation of goethite and showed that they may be related to the high mobility of organometallic complexes of iron and aluminum through water percolation. Also, Craig and Vaughan (1981), Bosch *et al.*

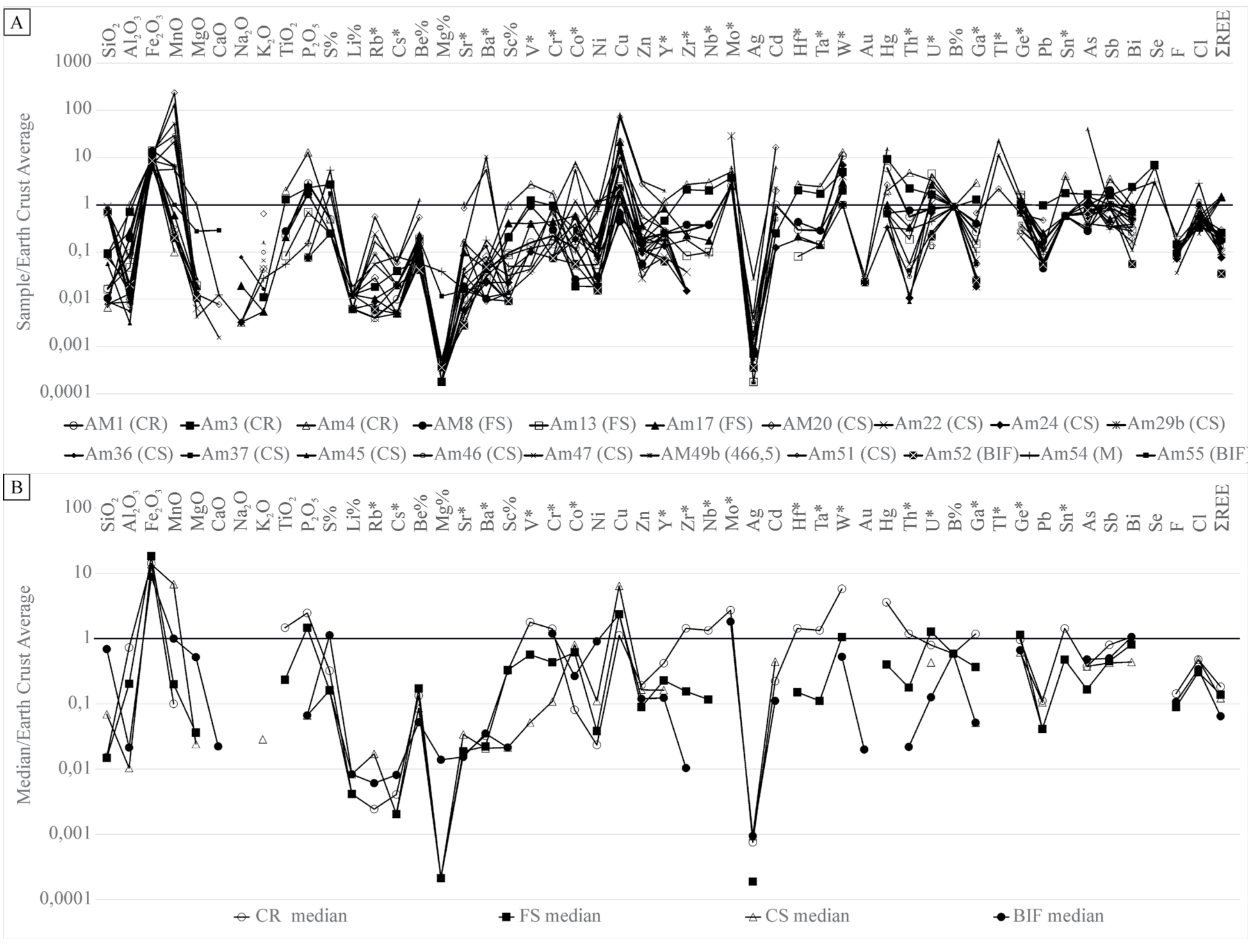

CR: crust; FS: fine saprolite; CS: coarse saprolite; M: mafic rock; *see Table 1.

Figure 11. The chemical element concentrations of all analyzed samples representing the distinct horizon at S11D iron deposit normalized to Earth Crust average after Rudnick and Gao (2003). (A) Normalization by each sample. (B) Normalization by the median of samples on each horizon.

(2010), and Das *et al.* (2011) proposed that colloids are precipitated locally as ferrihydrite ($Fe_2O_3 \cdot 0.5H_2O$) because of meteoric water circulation. The source of Fe to form goethite in this case is probably derived from the upper part of the profile, where hematite is partly dissolved forming "ghost"-crystals, preserving only the ancient hematite border (Figs. 7C and 7D).

Some impurities are related with the formation of goethite. Normally, the cut-off grade used for the iron ore is 60 wt. % Fe, with impurities of < 2.0 wt.% MnO, 2–2.5 wt.% SiO_2 and Al_2O_3, and 0.2 wt.% P_2O_5 (Figueiredo e Silva *et al.* 2011). CVRD (1996) showed that the contaminants are found:

- in contact with "canga" (aluminum and phosphorous);
- in contact with lower basaltic wall rocks (particularly manganese);
- generally with increasing depth and silica content.

The newly formed minerals in the "canga" are Al-goethite (Fig. 7D) and gibbsite, which may contribute to the deleterious aluminum in the iron ore (0.05 to 16.2 wt.%), as well as P in probable aluminum-phosphates (0.01 to 1.68 wt.% P_2O_5). The hypogene cryptomelane and hollandite (Fig. 6F) can be related to the original stratigraphic variation in the BIF composition with MnO variations in the coarse saprolite (Costa *et al.* 2005b, Costa *et al.* 2013, Requelme 2013, Costa 2015).

Schellmann (1986) proposed the SiO_2, Fe_2O_3, and Al_2O_3 triplot method, which uses the major oxide elements for classifying the weathering products, and for comparing them with the protore composition, in order to determine the degree of supergene weathering that occurs within a laterite weathering profile. This method quantifies three levels of lateritization (e.g., strong, moderate, and weak). Only two main groups have been differentiated with similar compositions in the S11D samples: the BIFs and the iron ore (Fig. 14).

The mobility of the chemical elements through the regolith was analyzed based on the normalization of major oxide element and trace element composition via the average of the UCC (after Rudnick & Gao 2003) and average BIF composition (after Macambira & Schrank 2002) (Tab. 1). According to Costa *et al.* (2014), the absolute enrichment occurs when element factors exceed the maximum values recorded for Al (3.0) and Ti (2.8) plus 50%, *i.e.*, 4.5 and 4.2, respectively. Factors 1 to 4.5 correspond to relative enrichment (precipitation in situ), factor < 1.0 correspond to leaching, and absolute enrichment to a factor of up to 10.1 (Costa *et al.* 2014). Considering these factors, Fe_2O_3 is the only main major oxide with a mobile behavior, as it was captured locally, related to the precipitation of the newly formed goethite in the iron crust and in many parts of the saprolite. The Al_2O_3 and TiO_2 are immobile (factor

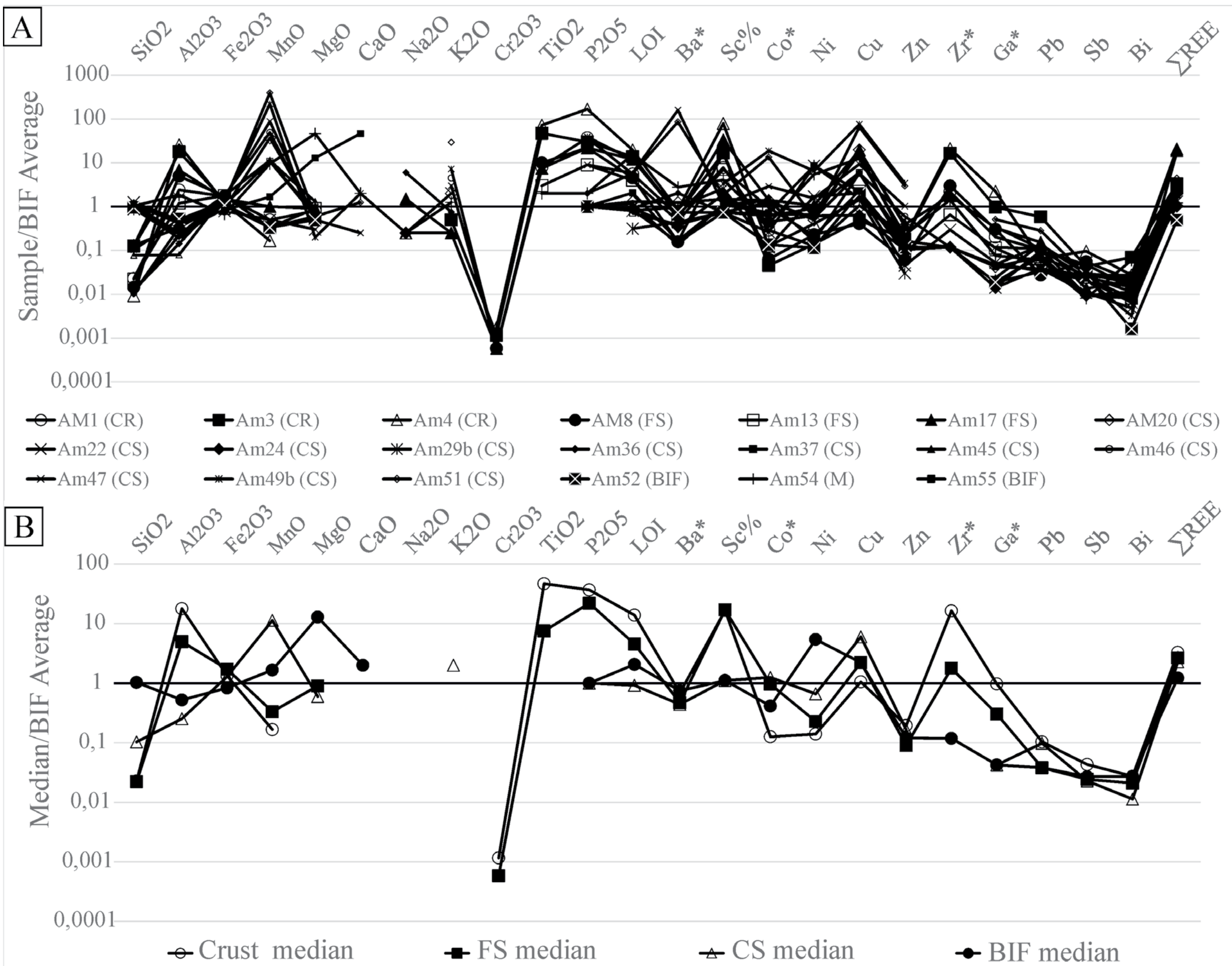

CR: crust; FS: fine saprolite; CS: coarse saprolite; M: mafic rock; *see Table 1.

Figure 12. The chemical element concentrations of all analyzed samples at S11D iron deposit normalized after Carajás banded iron formation (BIF) average composition after Macambira and Schrank (2002) and Macambira (2003). (A) Normalization by each sample. (B) Normalization by the median of samples on each horizon.

approximately 4.0), denoting a relative enrichment (residual). However, SiO_2 is mobile (in addition to MgO, CaO, Na_2O, and K_2O), because they were moved in the laterite profile, from the protore into the FS and crust (CR). The locally high content of Al and P is probably related to the weathering of mafic dikes (Costa *et al.* 2013), which are the primary source for the formation of kaolinite, gibbsite, and Al-goethite.

The trace elements Co, Ni, Cu, Cd, and Zn are depleted in the FS and CR (Fig. 11B). Moreover, they show a positive correlation with S (r = 0.30), Mo (r = 0.69), Cr (r = 0.42) in the protolith samples. It appears reasonable that sulfides located in the mafic rocks are the most probable source of those mobile elements, although other minerals cannot be ruled out. During their mobilisation, they can form oxyanions in solution, which would be readily adsorbed on iron oxy-hydroxide surfaces at low pH levels expected to prevail in the oxidized weathering environment (Dixit & Hering 2003, Stollenwerk 2003, Mitsunobu *et al.* 2010).

The granitophile elements (Mo, W, U, and Sn) are enriched in the FS and CR (Fig. 11). Macambira and Schrank (2002) showed that these elements display low concentrations in BIFs of the CMP or are below detection limit (Fig. 12). The complex signature of the trace elements within the iron oxides could be the result of variations in the local settings (granite intrusions, ~1.8 Ga) over the BIFs (Dall'Agnoll & Oliveira 2007).

The REE, Th, U, Y, Hf, Ta, Nb, Sc, and Zr show a strong positive correlation with each other. They are commonly related to residual minerals (*i.e.*, zircon — Fig. 10B and anatase — Fig. 10F), which are insoluble and usually immobile under surface conditions (Jiang *et al.* 2005, Santos *et al.* 2016). Furthermore, the distribution curves of the chondrite normalized REE values show the geochemical signature of BIF (Fig. 13). Europium shows strongly pronounced positive anomalies in most of the samples. McDaniel *et al.* (1994) explained that the positive Eu anomalies occur due to intense surface weathering, which is caused by a strongly oxidizing environment, removing preferentially most LREE. Also, Braun *et al.* (1990) showed that Ce is removed less readily from the system when oxidized to Ce^{4+} because of its incorporation into insoluble hydroxides and oxides (*i.e.*, cerianite).

The genetic laterite-supergene iron ore model for the S11D deposit in Carajás Mineral Province

The dissolution of quartz/chert bands occurred during the first stage of weathering (Fig. 15A) and is characterized by the absorption of water molecules on the solid silanol surface.

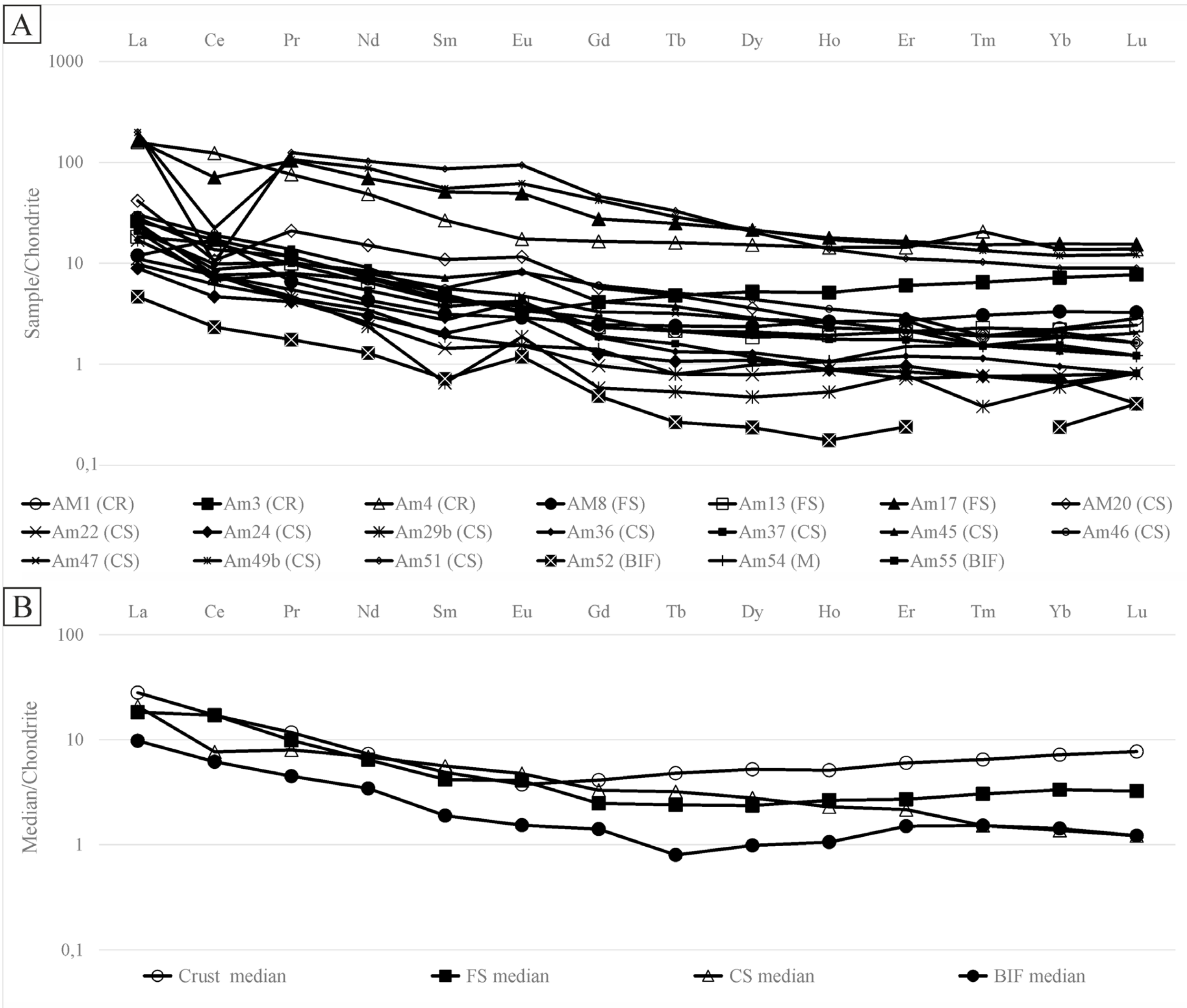

CR: crust; FS: fine saprolite; CS: coarse saprolite; JP: jaspilite; M: mafic rock.

Figure 13. Rare earth element distribution in S11D samples normalized to chondrites after Barrat *et al.* (2012). (A) Normalization by each sample. (B) Normalization by the median of samples on each horizon.

This caused the release of orthosilicic acid (H_4SiO_4) into solution (Sokolova 2013).

The second stage is characterized by the oxidation of magnetite (Fig. 15B), which produced a range of porous iron ore types. The ore quality ranges from martite (oxidized magnetite) to microplaty hematite (Fig. 15C). However, there is a high probability that the second stage is synchronous with the first stage.

The weathering of the chert bands with the formation of cavities, and later cementation by goethite, forms a typical hard cap (iron crust) on the top of the deposit (Fig. 15D). Groundwater movement leached the silica to produce porous ore. The typical plateaus of the deposits today are interpreted as the result of the resistance of the iron crust to erosion.

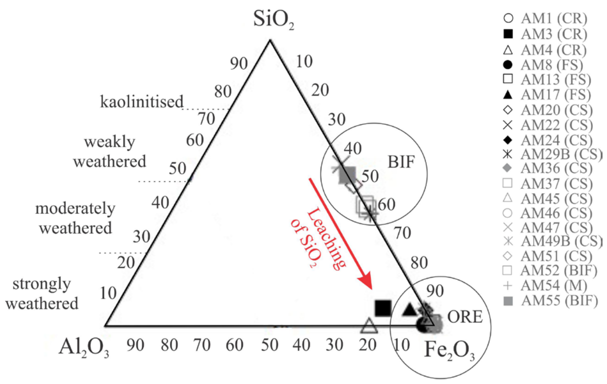

CR: crust; FS: fine saprolite; CS: coarse saprolite; M: mafic rock.

Figure 14. Ternary diagram (SiO_2, Fe_2O_3, Al_2O_3) of S11D samples. Areas circled correspond to the range of banded iron formation (BIF) protore composition. Limits of lateritization for typical laterite profiles determined according to the calculation of Schellmann (1986).

The input of small amounts of alumina, from the weathered mafic dikes, into this Fe–Si system may have caused significant modifications in the weathering profile. The most significative modification is observed at the top of the fine saprolite horizon, which has a suite of aluminous minerals (Al-goethite, kaolinite, and gibbsite) covering the orebody.

Ramanaidou (2009) showed that weathered dikes assist to increase the volume of water percolating through the profile and, in turn, accelerate the rate of quartz dissolution. In contrast, the hypogene iron oxides near the dikes are as much unweathered as hypogene iron oxides at depth below the water table. Therefore, the increase in water flow cannot explain, by itself, the more intense weathering of the hypogene oxides.

Ramanaidou *et al.* (2003), Morris and Ramanaidou (2007), and Ramanaidou (2009) proposed that small amounts of aluminum actively enhance the weathering by precipitating gibbsite and by combining with iron to form supergene aluminum-rich goethite. In addition, when gibbsite [$Al(OH)_3$] precipitates from aluminum-rich solution, it releases protons generating a local acidic environment, where hypogene iron oxides dissolve releasing iron cations into the solution, which in turn reacts with aluminum to form aluminum-rich goethite (Fig. 15D).

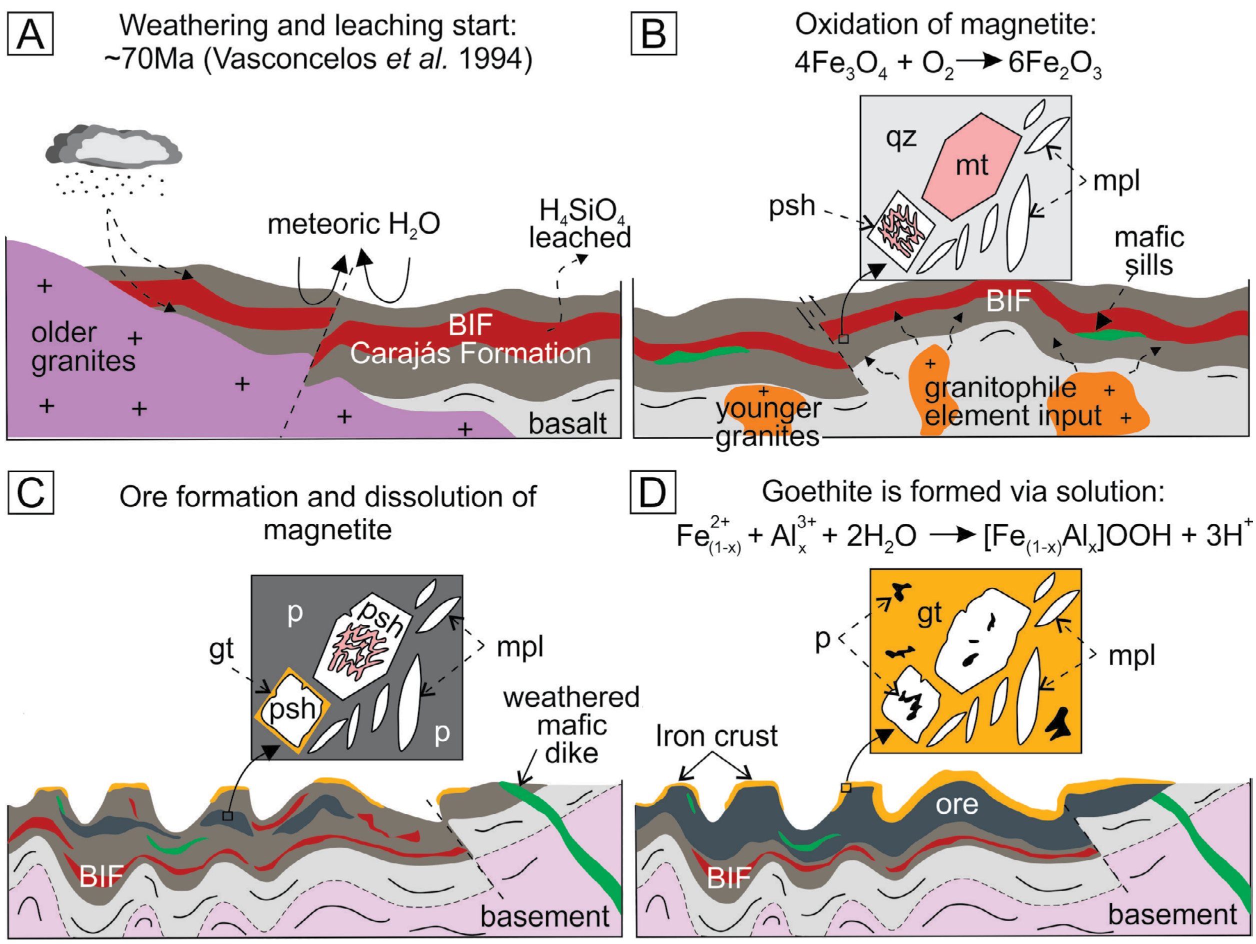

mt: magnetite; qz: quartz; psh: hematite pseudomorph after magnetite; gt: goethite; mpl: microplaty hematite; p: porosity.

Figure 15. Genetic laterite-supergene iron ore model for the S11D deposit in the Carajás Mineral Province.

CONCLUSIONS

The genesis of BIF-derived lateritic iron ores in the S11D deposit consists mainly of dissolution of quartz/chert bands, oxidation, fracturing, collapse, and hydrolyzes of some primary silicates and neoformation of iron-aluminum minerals, such as Al-goethite and gibbsite. The weathering history starts with the oxidation of the magnetite crystals into hematite, initially preserving the volume of weathered BIF. The decomposition of quartz/chert and leaching of silica has increased the porosity, generating a range of highly porous iron ores. The loss of the volume caused breaking and collapse of the iron bands, whereas quartz was almost completely leached out in the saprolite horizon. The iron crust caps the weathering profile, containing martite and microplaty hematite, cemented by goethite.

The hypogene iron minerals are the source for the newly formed minerals. The newly formed minerals form a sub-horizon on the top of the fine saprolite horizon, characterized by iron-aluminum oxides, where the primary crystallographic structure has been highly modified. The alumina influx was greatly favored by weathering processes of mafic dikes. Alumina caused the acceleration of degradation processes in this iron-rich environment.

The sequence of iron ore studied in the S11D mine, which is reflected in a complete, mature laterite profile, can be well correlated with other iron ore-bearing lateritic profiles in Carajás, such as the N8, N5, N4, N1 deposits, and in iron ore deposits in Australia, India and Africa. This relationship suggests that these sequences have experienced a similar supergene genesis and evolution.

ACKNOWLEDGEMENT

The authors would like to thank Conselho Nacional de Desenvolvimento Científico e Tecnológico (CNPq) (M.L.C. — grant number 304.519/2009-0 and 305014/2016-8 and A.C.S.S. — scholarship), Instituto Nacional de Ciência e Tecnologia – Geociências da Amazônia (INCT-GEOCIAM) (M.L.C. — grant number 573733/2008-2), and Instituto Tecnológico Vale — Universidade Federal do Pará/Fundação de Amparo e Desenvolvimento da Pesquisa (ITV-UFPA/FADESP) (M.L.C. — grant number 3753) for their financial support. The authors wish to acknowledge Vale S.A. for providing access to geological data and for the technical, logistic, and financial support. They are also grateful to the laboratories of Mineral Characterization and Microanalyses at the Geoscience Institute (UFPA). The authors would also like to thank Clovis Wagner Maurity (ITV) for his help, assistance, encouragement, and in numerous discussions.

ARTICLE INFORMATION
Manuscript ID: 20180128. Received on: 11/27/2018. Approved on: 03/10/2020.
A.S. wrote the main body of the manuscript and prepared the figures; M.C. provided advisorship regarding Carajás Province geology, revised and improved the manuscript through corrections and suggestions, proposed the genetic laterite-supergene model of S11D deposit, which resulted in Figure 15.
Competing interests: The authors declare no competing interests.

REFERENCES

Barrat J., Zanda B., Moynier F., Bollinger C., Liorzou C., Bayon G. 2012. Geochemistry of CI-chondrites: major and trace elements and Cu and Zn isotopes. *Geochimica et Cosmochimica Acta*, **83**:79-92. https://doi.org/10.1016/j.gca.2011.12.011

Bosch J., Heister K., Hofmann T., Meckenstock R.U. 2010. Nanosized iron oxide colloids strongly enhance microbial iron reduction. *Applied and Environmental Microbiology*, **76**(1):184-189. https://doi.org/10.1128/AEM.00417-09

Braun J.J., Pagel M., Muller J.P., Bilong P. Michard A., Guillet B. 1990. Cerium anomalies in lateritic profiles. *Geochemica et Cosmochimica Acta*, **54**(3):781-795. https://doi.org/10.1016/0016-7037(90)90373-S

Companhia Vale do Rio Doce (CVRD). 1996. Resumo dos aspectos geológicos da Província Mineral Carajás. *In*: DIGEB/DEPAB/GIMB/SUMIC. *Guia de excursão*, p. 392-403.

Costa L.C. 2015. *Minerais de manganês como contaminantes do minério de ferro na mina N5W em Carajás, Pará*. MS Dissertation, Instituto de Geociências, Universidade Federal do Pará, Belém, 87 p.

Costa L.C.G., Costa M.L., Farias H.D., Couto A., Galbiatti F., Braga M.A.S. 2013. Os minerais contaminantes do minério de ferro de N5W, Carajás-PA: oxi-hidróxidos de Mn e sílica. *In*: Simpósio de Geologia da Amazônia, 13., 2013. *Recursos minerais e sustentabilidade territorial na Amazônia*, p. 671-674.

Costa M.L. 1991. Aspectos geológicos dos lateritos da Amazônia. *Revista Brasileira de Geociências*, **21**(2):146-160.

Costa M.L., Araújo E.S. 1997. Caracterização mineralógica e geoquímica multi-elementar de crostas ferruginosas lateríticas tipo minérios de ferro em Carajás. São Paulo. *Geociências*, **16**(1):55-86.

Costa M.L., Carmo M.S., Behling H. 2005a. Mineralogia e geoquímica de sedimentos lacustres com substrato laterítico na Amazônia Brasileira. *Revista Brasileira de Geociências*, **35**(2):165-176.

Costa M.L., Cruz G.S., Almeida H.D.F, Poellmann H. 2014. On the geology, mineralogy and geochemistry of the bauxite-bearing regolith in the lower Amazon basin: evidence of genetic relationships. *Journal of Geochemical Exploration*, **146**:58-74. https://doi.org/10.1016/j.gexplo.2014.07.021

Costa M.L., Fernandez O.J.C., Requelme M.E.R. 2005b. O Depósito de Manganês do Azul, Carajás: estratigrafia, mineralogia, geoquímica e evolução geológica. *In*: ADIMB (ed.). *Caracterização de depósitos minerais em distritos mineiros da Amazônia*. p. 227-334.

Costa M.L., Leite A.S., Poellmann H. 2016. A laterite-hosted APS deposit in the Amazon region, Brazil: the physical-chemical regime and environment of formation. *Journal of Geochemical Exploration*, **170**:107-124. https://doi.org/10.1016/j.gexplo.2016.08.015

Costa M.L., Queiroz J.D.S., Silva A.C.S., Almeida H.D.F., Costa L.C.C. 2011. Perfil Laterítico Desenvolvido Sobre Formação Ferrífera Bandada (Jaspilito) em Carajás. *In*: Simpósio de Geologia da Amazônia, 12., 2011, Boa Vista. *Annals...*, p. 403-407.

Costa M.L., Sousa D.J.L., Angélica R.S. 2009. The contribution of lateritization processes to the formation of the Kaolin deposits from Eastern Amazon. *Journal of South American Earth Sciences*, **27**(2-3):219-234. https://doi.org/10.1016/j.jsames.2008.11.008

Craig J.R. and Vaughan D.J. 1981. Ore Microscopy and Ore Petrography. *John Wiley and Sons*, New York, **25**.

Dall'Agnoll R., Oliveira D.C. 2007. Oxidized, magnetite-series, rapakivi-type granites of Carajás, Brazil: Implications for classification and petrogenesis of A-type granites. *Lithos*, **93**(3):215-233. https://doi.org/10.1016/j.lithos.2006.03.065

Dall'agnol R., Oliveira D.C., Guimarães F.V., Gabriel E.O., Feio G.R.L., Lamarão C.N., Althoff F.J., Santos, P.A., Teixeira M.F.B., Silva A.C., Rodrigues D.S., Santos M.J.P., Silva C.R.P., Santos R.D., Santos P.J.L. 2013. Geologia do Subdomínio de Transição do Domínio Carajás – Implicações para a evolução arqueana da Província Carajás - Pará. *In*: Simpósio de Geologia da Amazônia, 13., 2013, Belém. *Annals*...

Dalstra H., Guedes S. 2004. Giant hydrothermal hematite deposits with Mg-Fe metasomatism: a comparison of the Carajás, Hamersley and other iron ores. *Economic Geology*, **99**(8):1793-1800. https://doi.org/10.2113/gsecongeo.99.8.1793

Dardenne M.A., Schobbenhaus C. 2001. O escudo do Brasil Central. *In*: *Metalogênese do Brasil*. Brasília, Ed. Universidade de Brasília/CPRM, p. 46-105.

Das S., Hendry J.M., Essilfie-Dughan J. 2011. Transformation of two-Line Ferrihydrite to Goethite and Hematite as a Function of pH and Temperature. *Environmental Science of Technology*, **45**(1):268-275. https://doi.org/10.1021/es101903y

Davis B.L., Rapp Jr. G., Walawender M.J. 1968. Fabric and structural characteristics of the martitization process. *American Journal Science*, **266**(6):482-496. https://doi.org/10.2475/ajs.266.6.482

Dixit S., Hering J.G. 2003. Comparison of arsenic(V) and arsenic (III) sorption onto iron oxide minerals: Implications for arsenic mobility: *Environmental Science and Technology*, **37**(18):4182-4189. https://doi.org/10.1021/es030309t

Figueiredo e Silva R.C., Hagemann S., Lobato L.M., Rosière C.A., Banks D.A., Davidson G.J., Vennemann T., Hergt J. 2013. Hydrothermal Fluid Processes and Evolution of the Giant Serra Norte Jaspilite-Hosted Iron Ore Deposits, Carajás Mineral Province, Brazil. *Economic Geology*, **108**(4):739-779. https://doi.org/10.2113/econgeo.108.4.739

Figueiredo e Silva R.C., Lobato L.M., Rosière C.A., Hagemann S. 2011. Petrographic and geochemical studies at giant Serra Norte iron ore deposits in the Carajás mineral province, Pará State, Brazil. *Geonomos*, **19**(2):198-223. https://doi.org/10.18285/geonomos.v19i2.54

Figueiredo e Silva R.C., Lobato L.M., Rosière C.A., Hagemann S.G, Zucchetti M., Baars F.J., Morais R., Andrade I. 2008. Hydrothermal origin for the jaspilite-hosted, giant Serra Norte iron ore deposits in the Carajás mineral province, Para State, Brazil. *In*: Hagemann S.G., Rosière C.A., Gutzmer J., Beukes N.J. (eds.), *BIF-related high-grade iron mineralization*. Society of Economic Geologists, v. 15, p. 255-290.

Grainger C.J., Groves D.I., Tallarico F.H.B., Fletcher I.R. 2008. Metallogenesis of the Carajás Mineral Province, southern Amazon Craton, Brazil: Varying styles of Archean through Paleoproterozoic to Neoproterozoic baseand precious-metal mineralization. *Ore Geology Reviews*, **33**(3-4):451-489. https://doi.org/10.1016/j.oregeorev.2006.10.010

Horbe A.C. & Costa M.L. 2005. Lateritic crusts and related soils in eastern Brazilian Amazonia. *Geoderma*, **126**(3-4):225-239. https://doi.org/10.1016/j.geoderma.2004.09.011

Jiang S.Y., Wang R.C., Xu X.S., Zhao K.D. 2005. Mobility of high field strength elements (HFSE) in magnetic-, metamorphic-, and submarine-hydrothermal systems. *Physics and Chemistry of the Earth*, **30**(17-18):1020-1029. https://doi.org/10.1016/j.pce.2004.11.004

Klein C., Ladeira E.A. 2002. Petrography and geochemistry of the least-altered banded iron-formation of the Archean Carajás Formation, northern Brazil. *Economic Geology*, **97**(3):643-651. https://doi.org/10.2113/gsecongeo.97.3.643

Lindenmayer Z.G., Laux J.H., Teixeira J.B.G. 2001. Considerações sobre a origem das Formações Ferríferas da Formação Carajás, Serra dos Carajás. *Revista Brasileira de Geociências*, **31**(1):21-28.

Macambira J.B. 2003. *O ambiente deposicional da Formação Carajás e uma proposta de modelo evolutivo para a Bacia Grão Pará*. PhD Thesis, Instituto de Geociências, Universidade Estadual de Campinas, Campinas , 217 p.

Macambira J.B., Schrank A. 2002. Químio-estratigrafia e evolução dos jaspilitos da Formação Carajás (PA). *Revista Brasileira de Geociências*, **32**(4):567-577.

McDaniel D.K., Hemming S.R., McLennan S.M., Hanson G.N. 1994. Resetting of neodymium isotopes and redistribution of REEs during sedimentary processes: The Early Proterozoic Chelmsford Formation, Sudbury Basin, Ontario, Canada. *Geochimica et Cosmochimica Acta*, **58**(2):931-941. https://doi.org/10.1016/0016-7037(94)90516-9

McLennan S.M. 1989. Rare Earth Elements in Sedimentary Rocks: Influence of Provenance and Sedimentary Process. *Review of Mineralogy*, **21**(1):169-200.

Meirelles M.R. 1986. *Geoquímica e petrologia dos jaspilitos e rochas vulcânicas associadas, Grupo Grão-Pará, Serra dos Carajás.* MS Dissertation, Universidade de Brasília, Brasília, 171 p.

Mitsunobu S., Takahashi Y., Terada Y., Sakata M. 2010. Antimony(V) incorporation into synthetic ferrihydrite, goethite, and natural iron oxyhydroxides. *Environmental Science & Technology*, **44**(10):3712-3718. https://doi.org/10.1021/es903901e

Morris R.C., Ramanaidou E.R. 2007. Genesis of the channel iron deposits (CID) of the Pilbara region, Western Australia. *Australian Journal of Earth Sciences*, **54**(5):733-756. https://doi.org/10.1080/08120090701305251

Oliveira S.B., Costa M.L., Prazeres Filho H.J. 2016. The Lateritic Bauxite Deposit of Rondon do Pará: A New Giant Deposit in The Amazon Region, Northern Brazil. *Economic Geology and the Bulletin of the Society of Economic Geologists*, **111**(5):1277-1290. http://dx.doi.org/10.2113/econgeo.111.5.1277

Ramanaidou E.R. 2009. Genesis of lateritic iron ore from banded iron-formation in the Capanema mine (Minas Gerais, Brazil). *Australian Journal of Earth Sciences*, **56**(4):605-620. https://doi.org/10.1080/08120090902806354

Ramanaidou E.R., Morris R.C., Horwitz R.C. 2003. Channel iron deposits of the Hamersley Province, Western Australia. *Australian Journal of Earth Sciences*, **50**(5):669-690. https://doi.org/10.1111/j.1440-0952.2003.01019.x

Requelme M.E.R. 2013. *Mineralogia e Química-Mineral dos Oxi-hidróxidos de Manganês do Depósito do Azul, Província Mineral de Carajás: A Importância da Série Criptomelana-Hollandita*. PhD Thesis, Instituto de Geociências, Universidade Federal do Pará, Belém, 173 p.

Rosière C., Chemale Jr. F. 2000. Brazilian iron formations and their geological setting. Revista Brasileira de Geociências. **30** (2):274-278. https://doi.org/10.25249/0375-7536.2000302274278.

Rudnick R.L., Gao S. 2003. Composition of the continental crust. *In*: Rudnick R.L., Holland H.D., Turekian K.K. (eds.), *The Crust. Treatise on Geochemistry*, 3, p. 1-64. Amsterdam, Elsevier.

Santos P.H.C., Costa M.L., Leite A.S. 2016. The Piriá aluminous lateritic profile: mineralogy, geochemistry and parent rock. *Brazilian Journal of Geology*, **46**(4):617-636. https://doi.org/10.1590/2317-4889201620160101

Schellmann W. 1986. A new definition of laterite. *In*: Banerji P.K. (ed.), Lateritization processes. *Memoir of the Geological Survey of India*, **120**:1-7.

Silva M.G. 2014. *Metalogênese das províncias tectônicas brasileiras*. Belo Horizonte, CPRM. 589 p.

Sokolova T.A. 2013. The destruction of quartz, amorphous silica minerals, and feldspars in model experiments and in soils: Possible mechanisms, rates, and diagnostics (the analysis of literature). *Eurasian Soil Science*. **46**:91-105. https://doi.org/10.1134/S1064229313010080

Stollenwerk K.G. 2003. Geochemical processes controlling transport of arsenic in groundwater: a review of adsorption. *In*: Welch A.H., Stollenwerk K.G. (eds.), *Arsenic in Groundwater*, p. 67-100. Boston, Kluwer Academic Publishers.

Tardy Y., Nahon D. 1985. Geochemistry of laterites stability of Al-goethite, Al-hematite and Fe^{+3}-kaolinite in bauxites and ferricretes: An approach to the mechanism of concretion formation. *American Journal of Science*, **285**:865-903.

Taylor D., Dalstra H.J., Harding A.E., Broadbent G.C., Barley M.E. 2001. Genesis of high-grade hematite orebodies of the Hamersley Province, Western Australia. *Economic Geology*, **96**(4):837-873. https://doi.org/10.2113/gsecongeo.96.4.837

Tolbert G.E., Tremaine J.W., Melcher G.C., Gomes C.B. 1971. The recently discovered Serra dos Carajás Iron Deposits, Northern Brazil. *Economic Geology*, **66**(7):985-994. https://doi.org/10.2113/gsecongeo.66.7.985

Vale S.A. 2017. *Form 20-F. Annual Report Pursuant to Section 13 Or 15(D) of the Securities Exchange Act of 1934*. Washington, United States Securities and Exchange Commission, 289 p.

Vale S.A. 2018. *Produção e vendas da Vale no 4T17*. Rio de Janeiro, Vale S.A. Available at: <http://www.vale.com/PT/investors/information-market/Press-Releases/ReleaseDocuments/2017%204Q%20Production%20Report_p.pdf>. Access on: Apr 11, 2018.

Varajão C.A.C., Ramanaidou E., Melfi A.J., Colin F., Nahon D. 1996. Martitização: alteração supergênica da magnetita. *Revista Escola de Minas*, **50**:18-20.

Vasconcelos P. M., Renne P.R, Brimhall G.H., Becker T.A. 1994. Direct dating of Weathering phenomena by $^{40}Ar/^{39}Ar$ and K-Ar analysis of supergene K-Mn oxides. *Geochimica et Cosmochimica Acta*, **58**(6):1635-1665. https://doi.org/10.1016/0016-7037(94)90565-7

Vasquez L.V., Rosa-Costa L.R., Silva C.G., Ricci P.F., Barbosa J.O., Klein E.L., Lopes E.S., Macambira E.B., Chaves C.L., Carvalho J.M., Oliveira J.G., Anjos G.C., Silva H.R. 2008a. Texto explicativo dos mapas geológico e tectônico e de recursos minerais do Estado do Pará. *In*: Vasquez M.L., Rosa-Costa L.T. (eds.), *Geologia e recursos minerais do Estado do Pará*. Sistema de Informações Geográficas –– SIG, escala 1:1.000.000. Belém, CPRM. 1 CD-ROM.

Vasquez M.L., Sousa C.S., Carvalho J.M.A. 2008b. *Mapa geológico e de recursos minerais do Estado do Pará, escala 1:1.000.000*. Programa Geologia do Brasil (PGB), Integração, Atualização e Difusão de Dados da Geologia do Estado do Brasil, Mapas Geológicos Estaduais. Belém, CPRM-Serviço Geológico do Brasil, Superintendência Regional de Belém. 1 CD-ROM.

White A. and Buss H. 2013. Natural Weathering Rates of Silicate Minerals. In: Treatise on Geochemistry: Surface and Groundwater, Weathering and Soils. *Elsevier Science Ltd.*, Editors: J. I. Drever, **7**(2):115-155. https://doi.org/10.1016/B978-0-08-095975-7.00504-0

Zhu J., Tang C., Li Z., Laipan M., He H., Liang X., Tao Q., Cai L. 2017. Structural effects on dissolution of silica polymorphs in various solutions. *Inorganica Chimica Acta*, **471**:57-65. https://doi.org/10.1016/j.ica.2017.10.003